Università degli Studi di Padova

Dipartimento di Fisica e Astronomia "Galileo Galilei"

Corso di Laurea in Fisica

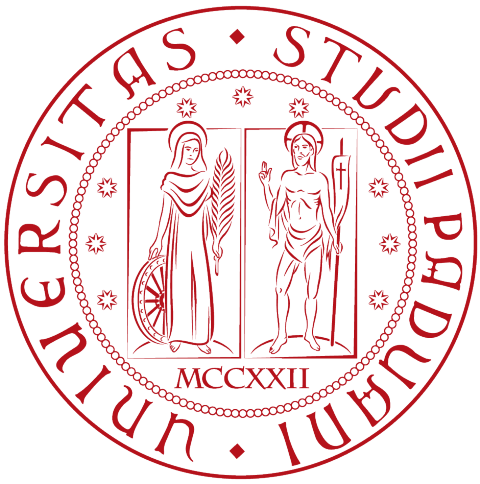

Search for Supernova Neutrinos with the JUNO detector.

Laureando:
Massimiliano Lincetto

Relatore:
Dott. Stefano Dusini
Controrelatore:
Prof. Daniele Gibin

Anno Accademico 2015/2016

Abstract

Observation of supernovae through their neutrino emission is a major fundamental field to understand both supernova dynamics and neutrino physical properties.

JUNO is a 35 kiloton scintillator detector, planned to start its activity in about 4 years in the Jiangmen region, China. It is based on an acrylic vessel with a diameter of 35 meters filled with an ultra-pure liquid scintillator and rigged with $\sim$ 18000 large (20") and $\sim$ 35000 small (3") photomultipliers. The primary aim of the experiment is to determine the neutrino mass hierarchy with a precise measurement of the oscillation of neutrinos produced in two nuclear reactors located at $\sim 50\,\mathrm{km}$ from the detector. In this thesis we analyze the detector structure and the proposed readout strategies and data acquisition architecture in order to evaluate the performance in the case of a supernova burst having a much higher event rate with respect to the nuclear reactor flux.

Taking advantage of an existing Monte Carlo software developed by the JUNO collaboration for the simulation of the supernova neutrino flux at the detector, in this thesis we build a complete framework implementing a GEANT4 simulation of JUNO that is used to simulate the detector response to the supernova neutrino interactions.

By means of this framework we characterize the response of the JUNO detector to a neutrino SN burst in terms of detection rate and neutrino energy reconstruction. In particular we study the behaviour of the 3" PMT system which thanks to the faster readout is the most suitable for the acquisition of an high-rate event as a supernova burst. Using simulated data we evaluate a possible analysis strategy to reconstruct the SN neutrinos flux and its time distribution. The efficiencies of different SN neutrino detection channels are evaluated and presented in the thesis.

Where existing data from SN neutrino consists only of the 24 neutrino events detected from SN1987A, the detection in JUNO of a supernova from a progenitor at 10 kpc will yield $\sim 5 \times 10^3$ inverse beta decay events from electron antineutrinos, plus several hundreds on other CC and NC interaction channels from all neutrino species.

Contents

1 Supernova Neutrinos **3**
- 1.1 SN overview and classification . . . 3
- 1.2 Core-collapse SN rate . . . 5
- 1.3 Core-collapse dynamics . . . 6
- 1.4 Neutrino emission . . . 10
- 1.5 SN1987A . . . 12
- 1.6 Neutrino astrophysics . . . 13
  - 1.6.1 Flavor conversion and mass hierarchy . . . 13
  - 1.6.2 Neutrino mass . . . 14
  - 1.6.3 Neutrino mixing . . . 15
  - 1.6.4 CP violation . . . 15
- 1.7 Supernova Early Warning . . . 16

2 SN neutrino detection in liquid scintillator **17**
- 2.1 Neutrino flux model . . . 17
  - 2.1.1 Survival probability . . . 17
  - 2.1.2 Flux dataset . . . 18
- 2.2 Detection channels . . . 18
  - 2.2.1 Inverse Beta Decay . . . 20
  - 2.2.2 Elastic scattering . . . 23
  - 2.2.3 Superallowed NC interaction . . . 25
  - 2.2.4 Superallowed CC interactions . . . 26

3 JUNO scintillation detector **29**
- 3.1 Liquid scintillator . . . 29
  - 3.1.1 Signal time profile . . . 30
- 3.2 Photomultiplier configuration . . . 31
- 3.3 Readout strategies . . . 33
  - 3.3.1 Readout electronics . . . 34
  - 3.3.2 Photomultiplier dark noise . . . 35

4 Simulation framework **36**
4.1 JUNO supernova generator 36
4.2 JUNO detector Monte Carlo simulation 36
4.3 Software development 37

5 Analysis **38**
5.1 Characterization of the signal 38
5.2 Time profile of the signal 39
5.3 SPMT dark noise 39
5.4 Background estimation 40
5.5 Simulation of the detector response 40
5.5.1 Inverse beta decay 41
5.5.2 Proton elastic scattering 41
5.5.3 ^{12}C NC excitation 42
5.5.4 Electron elastic scattering 43
5.5.5 Superallowed CC interactions 44
5.6 Event rates and channel efficiencies 44
5.7 Energy calibration and resolution 45
5.8 Reconstructed spectra 46
5.9 Data rate 46
5.10 Asynchronous vs synchronous trigger 47
5.11 Supernova trigger strategies 51

6 Conclusions **57**

Bibliography **58**

Chapter 1

Supernova Neutrinos

Supernovae (SNe) are explosions that may occur when a star reaches the end of its life, ejecting in the surrounding space matter in the order of a few solar masses ($M_\odot$) and energy in the order of 10^{51} erg.

After the convention established by F. Zwicky and his collaborators when pioneering the studies of supernovae in early 1930s [1], these events are designated by the SN prefix followed by the year of discovery and a progressive upper case letter (e.g. SN1987A).

1.1 SN overview and classification

In observational astronomy, the supernova classification is spectroscopic and depends on the composition of the observable envelope. The main distinction between type I and type II supernovae is based respectively on the absence or presence of hydrogen. Type I SNe are further distinguished in type Ia and type Ib/Ic depending on the presence of the absorption lines of silicon in the spectrum.

The optical properties of the envelope have little relevance to the neutrino astrophysics, as the neutrino emission pattern is produced by the explosion dynamics at the earlier stages when the envelope is still opaque to visible light. As for the explosion mechanism, type Ia SNe are generated from the thermonuclear explosion of a white dwarf, while type Ib/Ic/II SNe are generated by a characteristic *core-collapse* mechanism. The two types can be distinguished by the observation of the inner region that becomes visible a few months after the luminosity peak, when the ejecta become optically thin: its spectrum is dominated by the iron emission line for thermonuclear SNe in contrast to carbon and oxygen for core-collapse SNe.

The SNe of type Ia are the result of the thermonuclear explosion of a carbon-oxygen white dwarf. The white dwarf is the final stage of a star that reaches the end of the thermonuclear fuel burning, holding a mass of about $1M_\odot$ and a radius of $\sim 5000\,\mathrm{km}$, resulting in a density of $\sim 10^6\,\mathrm{g/cm^3}$. The

white dwarf is stable as long as the pressure of the degenerate electrons can balance the gravitational force [2]: this condition is satisfied up to a limit called the *Chandrasekhar mass* and is dependent on the electron density which in turn depends on the proton fraction in the star composition. In the case of a typical proton fraction of $Y_e = 0.5$ the Chandrasekhar mass is $\sim 1.4 M_\odot$. If the white dwarf has a close companion star from which it can gain mass beyond the Chandrasekhar limit, it becomes unstable and starts the fusion of carbon and oxygen into heavier nuclei, releasing high amounts of energy that eventually lead to a thermonuclear explosion [3]. A type Ia SN leaves behind an expanding nebula and no compact remnant, its optical spectrum is characterized by silicon which is one of the products of the carbon-oxygen fusion and by ^{56}Fe which is the last stage of the $^{56}\text{Ni} \longrightarrow {}^{56}\text{Co} \longrightarrow {}^{56}\text{Fe}$ decay chain. There is little variability in the process producing type Ia SNe, as a consequence they all have almost identical characteristics and predictable observable properties: an empirical relation between the luminosity and duration of the light peak was discovered by Phillips in 1993 [4] and allows for the exploiting of these events as *standard candles* (i.e. unit of measure for luminosity) for SN events within a radius of 100 Mpc.

Supernovae of type Ib, Ic and II originate instead from the collapse of massive stars with $M \gtrsim 8 M_\odot$ and usually leave behind a compact remnant in the form of neutron star with a mass up to 2 $M_\odot$, detectable as a pulsar. Neutrinos are emitted in a time window of few seconds after the collapse of the core of the star, when the envelope is still optically thick and traps inside the electromagnetic radiation. Under this circumstances, $\sim$ 99% of the original gravitational energy (3×10^{53} erg) is released through the emission of $\sim 10^{58}\, \nu$ on a 10 MeV energy scale. The number of neutrinos is one order of magnitude greater than the original lepton number of the star core. Type II supernova are believed to be the product of the collapse of red and blue giant stars having a mass between 8-9 and 40-60 $M_\odot$. The core-collapse of progenitor stars with the same initial mass is subject to a wide variability in the observable result, depending on the size and the mass of the hydrogen envelope. Core-collapse SNe are further classified - but this is not a rigid classification since many intermediate cases exist - depending on their optical properties [5]:

- Ib: no H envelope;
- Ic: no H and no He envelope;
- IIL: linear decrease of luminosity over time;
- IIP: the light curve shows a plateau (envelope mass between 5 and 10 $M_\odot$ and radius $\sim 10^{15}$ cm, usually fainter than IIL);
- IIF: the supernova is faint;

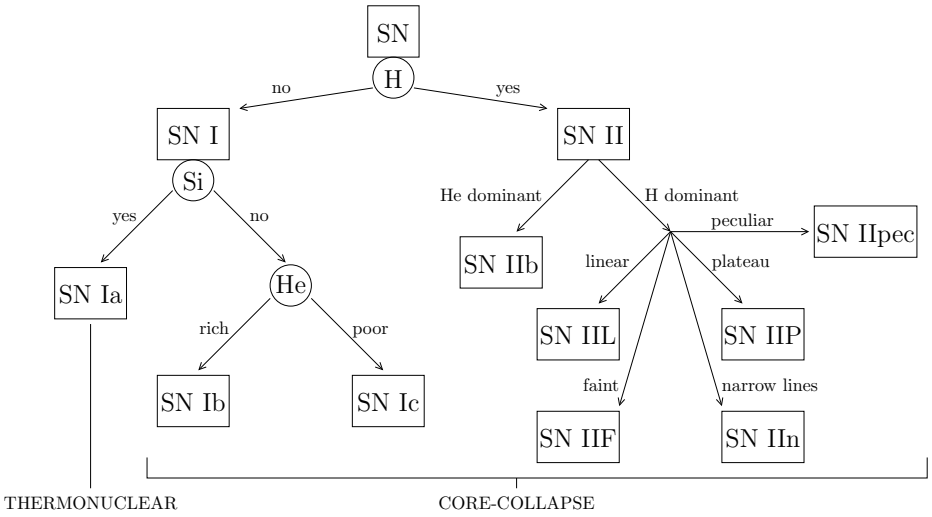

Figure 1.1: Supernova classification based on the optical properties [6].

- IIb: He emission dominates over H
- IIn: the spectrum exhibits narrow lines;
- IIpec: the supernova is *peculiar*.

The shockwave that is produced in a core-collapse process ionizes the hydrogen envelope and causes the ejection of matter in the surrounding space. The following hydrogen recombination has a stabilising effect on the photosphere temperature and radius, giving a luminosity plateau which is dependent on the mass of the envelope. If the mass is too low ($\lesssim 1 - 2M_{\odot}$) no plateau is observed and the SN exhibits a linear decrease of luminosity.

From now on we will focus on core-collapse supernovae only, as we are interested in their neutrino signature.

1.2 Core-collapse SN rate

The estimates of supernova rates estimates are based on astronomical observation. No core-collapse SNe of type IIb/c and II are observed in elliptical galaxies which, being older, are less subject to star formation processes that can lead to the production of short-lived massive stars. While in studies conducted in the last 40 years the estimates for core-collapse events within the Milky Way range from one to ten events per century [7], the most recent results point to a value between one and two [8]. The lack of observation of core-collapse SNe by the Baksan Underground Neutrino Observatory since

its start of operations in June 1980 allows to put an upper constraint of 13 SNe per century at the 90% CL, however with large uncertainties [9].

The rate of core-collapse SN allows also for the estimation of the *Relic Supernova Neutrino Background* (RSNB), i.e. the neutrino background from all the past core-collapse events. The study conducted by SuperKamiokande searched for neutrinos above the energy threshold of 19.3 MeV and its lack of observation has constrained the $\overline{\nu}_e$ flux to $\Phi_{\overline{\nu}_e} < 1.2\,\mathrm{cm}^{-2}\mathrm{s}^{-1}$ [10].

1.3 Core-collapse dynamics

A comprehensive treatment of current SN core-collapse models, of which we will here give a summary, can be found in reference [11]. In a typical core-collapse SN explosion, energy in the order of 3×10^{53} erg is released and carried away mainly by the neutrino emission, while only a small fraction is released at a later time with the ejection of matter (1%) and electromagnetic radiation (0.01%).

The core-collapse mechanism takes place at the end of the life of stars with a mass between 8-9 and 40-60 $M_\odot$: as the core collapses to form a proton-neutron star, the rebound shockwave that is produced leads to the explosion of the star. The exact dynamics of the process is still debated and is double-tied to the neutrino physical properties. The initial mass and the metallicity of the star play a fundamental role in determining the outcome of a core-collapse [12], as it is summarized in figure 1.2.

The metallicity is defined as the fraction of heavy elements (such as iron and other metals) in the star composition. It influences the optical opacity of the envelope and thus the inner concentration of photons that can participate in processes linked to the onset of the collapse, as we will examine later in detail.

The initial mass strongly influences the final evolution stages of the life of the star. On the low end of the SN progenitor mass range, the stars with $M < 9M_\odot$ will collapse to a white dwarf which is stable unless it belongs to a multiple system and can gain mass from a companion, eventually producing a thermonuclear SN. On the opposite end, the stars with $M > 40M_\odot$ are subject to significant loss of mass through the production of stellar winds, ending up with small envelopes which are opaque enough for the triggering of a core-collapse process only at high values of metallicity. A different process involves the stars between 25 and 40 $M_\odot$ with low-to-mid metallicity: they undergo a first collapse to a proton-neutron star producing a SN IIp, then a second collapse to a black hole as the envelope falls back into the core.

A star with a mass over $10M_\odot$ will go through all the stages of nuclear fusion (H, He, C, O, Ne, Si) ending with an iron core of $\sim 1M_\odot$ surrounded by shells of lighter elements in an onion-like structure, as shown in figure 1.3. The iron core has a radius of a few thousands km (thus a density of

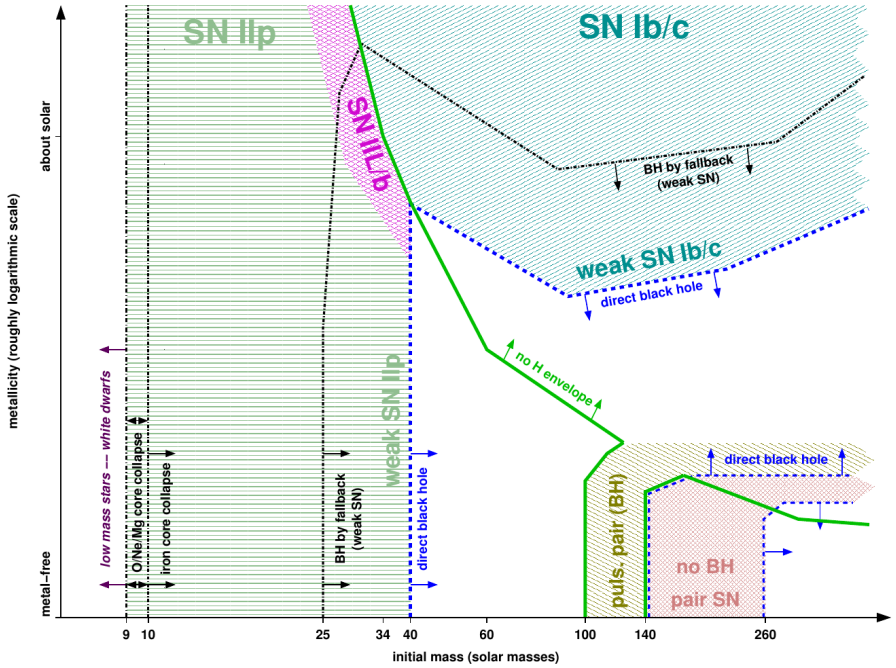

Figure 1.2: Prediction of the end of life of a star as a function of initial mass and metallicity [12].

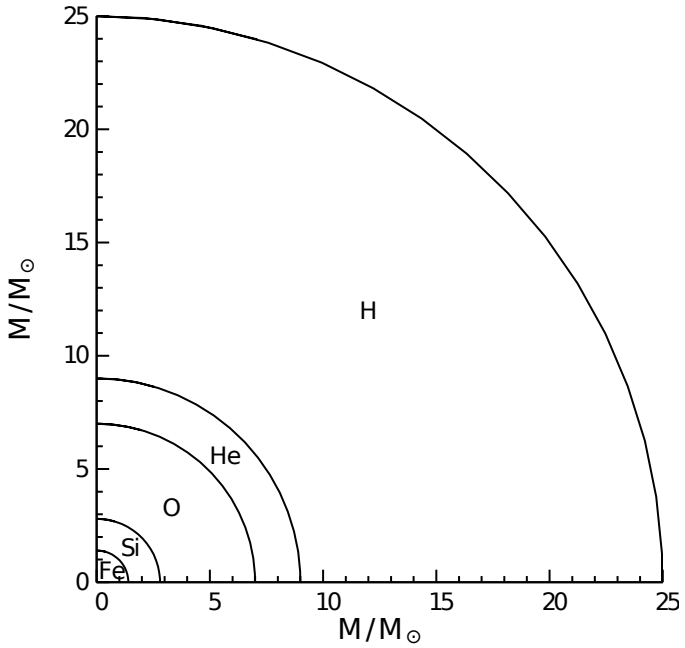

Figure 1.3: Onion-like structure for a $25M_{\odot}$ population I star before the collapse [6], the main element for each shell composition is represented, however several other elements are contained in each shell.

$10^{10}\,\mathrm{gcm}^{-3}$) and is sustained by the pressure of degenerate relativistic electrons at the MeV energy scale. At this point, iron is stable cannot participate in further nuclear fusion reactions but it is subject to photodissociation through the process:

$$\gamma(124\,\mathrm{MeV}) + {}^{56}\mathrm{Fe} \rightarrow 13\alpha + 4n$$

Protons, free or bound, are subject to the electron capture process:

$$e^{-} + p \rightarrow n + \nu_e$$

The result of the two is a progressive reduction of the electron number (and pressure) that eventually brings the star to the Chandrasekhar limit at which the core starts to collapse, increasing both temperature and density and thus further favouring the rate of the two reactions.

For stars between 9 and 10 $M_{\odot}$ the mechanism producing the iron core is slightly different: while hydrogen, helium and carbon are burnt in nuclear fusion, the star is too cold to burn oxygen nuclei. Under this circumstances it is the participation of neon and magnesium in the electron capture process that eventually leads to the onset of the collapse. Only the following increase in density can trigger the fusion of oxygen, neon and magnesium into iron.

In both cases, the phase before the onset of the collapse is called *capture* phase and its signature is a luminosity ramp in the electron antineutrino channel, with a non-thermal distribution growing from 12 to 16 MeV [13]. The luminosity rises to $\sim 10^{53}$ erg/s for a brief time of about 10 ms releasing energy in the order of 10^{51} erg. The capture process goes on until the inner part of the core ($\sim 0.8 M_{\odot}$) reaches a density of about 3×10^{11} g/cm^3 trapping the neutrinos inside. At this point, the star is divided in two parts: the inner core is undergoing a subsonic collapse with a velocity proportional to the radius, while the outer core is collapsing at a supersonic free-fall regime. Approximately one second after the onset, the inner core reaches the density of nuclear matter (10^{14} g/cm^3) and the pressure of degenerate nucleons abruptly stops the collapse settling in hydrostatic equilibrium and forming a proton-neutron star with a radius of 10 km. The matter which is still collapsing bounces on the proto-neutron star producing a supersonic shockwave that travels through the iron shell at a speed of 100 km/ms. The shock wavefront abruptly decelerates the infalling gas, producing a shocked mantle with a radius of 100 km and a density gradient that goes from the density of nuclear matter at the core to a value of 10^9 g/cm^3 on the outer surface.

During the shock propagation, about 1.5×10^{51} erg per $0.1 M_{\odot}$ are dissipated in the photodissociation of nuclei with the release of free nucleons behind the shock. The protons can participate in the electron capture process, producing both neutrons and a large number of electron neutrinos that pile up behind the shock, opaque to them as long as its density is above 10^{11} g/cm^3. A few milliseconds after the bounce the *shock breakout* takes place and neutrinos are released in the so-called *neutronization burst* or *breakout pulse*. In this phase of the neutrino emission the supernova reaches a luminosity of 6×10^{53} erg/s releasing another 10^{51} erg of energy in a time interval of a few milliseconds.

Different models have been proposed to explain the following explosion mechanism, depending upon the progenitor mass and the equation of state of the nuclear matter. If the shock, despite being weakened during the propagation, retains enough energy to expel the star envelope we have the *prompt* explosion scenario on a $\sim$ 100 ms time scale. Otherwise, as it is most likely to happen for stars above $10 M_{\odot}$, the shock stalls at a 200-300 km radius after $\sim$ 100 ms, while the matter keeps falling through and undergoing photodissociation in the so-called *accretion phase*. Under these conditions, the possible revival of the shock can lead to the SN *delayed* explosion scenario on a time scale of $\sim$ 0.5 s. The exact mechanism that triggers the revival is still controversial, but it is believed to be the result of concurrent effects of energy deposition from the thermal neutrinos, convective motions in the mantle and possibly acoustic power from oscillations of the protoneutron star in the accretion phase. One possible alternative to the supernova scenario is the collapse of the core into a black hole that occurs if the pressure of

degenerate nucleons cannot sustain the equilibrium as the mass of the core increases.

1.4 Neutrino emission

As we have seen, there are two neutrino emission stages in the early evolution of the supernova, the first being the *capture* phase at the onset of the collapse, the second being the *neutronization burst*. Both emissions occur over a brief time and cannot carry away significant amounts energy or lepton number from the star. The main portion of the energy is carried away by the subsequent thermal emission of the core, starting from the accretion phase, in the few seconds after the onset of the collapse.

We here summarize neutrino-producing processes in the core that occur at a temperature of 40 MeV:

- electron pair annihilation: $e^- + e^+ \rightarrow \nu + \overline{\nu}$
- electron-nucleon bremsstrahlung: $e^\pm + N \rightarrow e^\pm + N + \nu + \overline{\nu}$
- nucleon-nucleon brehmsstrahlung: $N + N \rightarrow N + N + \nu + \overline{\nu}$
- plasmon decay: $\gamma \rightarrow \nu + \overline{\nu}$
- photoannihilation: $\gamma + e^\pm \rightarrow e^\pm + \nu + \overline{\nu}$
- electron capture: $e^- + p \rightarrow n + \nu_e$
- positron capture: $e^+ + n \rightarrow p + \overline{\nu}_e$

Neutrinos are trapped inside the core and the mantle as long as the density is above $10^{11}\,\mathrm{g/cm^3}$. The surface of last scattering for neutrinos - from which they radiate - is called *neutrinosphere* and its radius depends on the neutrino cross section which in turn is function of both flavor and energy. Electron neutrinos and antineutrinos are distinguished from the other flavors since they are the only participating in charged current interactions that dominate the cross section at this energy scale. Plus, the higher concentration of neutrons over protons results in a higher interaction rate for electron neutrinos with respect to antineutrinos. We can therefore distinguish three energy-dependent neutrinospheres, that form at a radius between 50 and 100 km, for three groups of neutrinos starting from the deeper: $\nu_x = \{\nu_\mu, \overline{\nu}_\mu, \nu_\tau, \overline{\nu}_\tau\}$, $\overline{\nu}_e$ and ν_e. The higher cross section of a neutrino species is related to a larger neutrinosphere radius and to a colder emission, as the last scattering conditions take place at a lower energy. The average energies that can be estimated for ν_e, $\overline{\nu}_e$ and ν_x are respectively of 10, 15 and 20 MeV. Each neutrinosphere emits a flux with a blackbody-like thermal spectrum subject to a pinching (i.e. suppression of the tails) given by the energy dependence of the cross section.

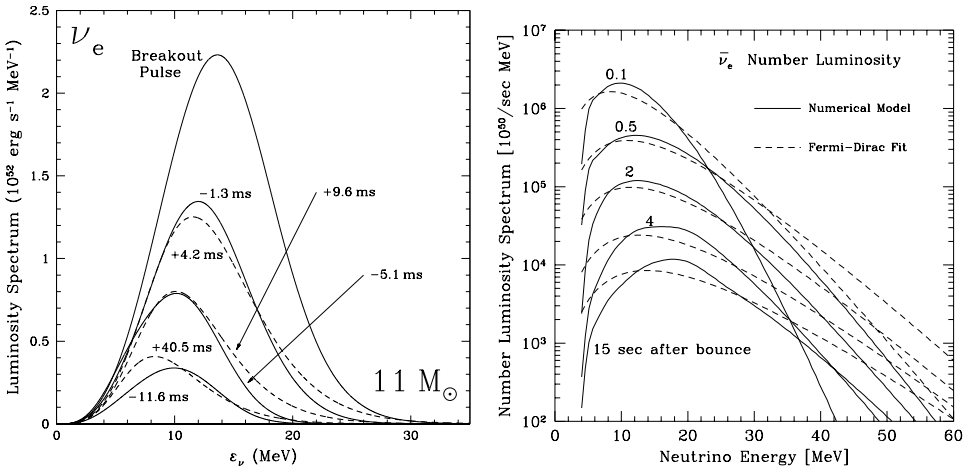

Figure 1.4: Left: luminosity spectrum of ν_e at different times referenced to the breakout pulse for a 11 $M_\odot$ progenitor [14]. Right: energy spectrum of $\overline{\nu}_e$ at different times after the bounce in terms of number luminosity, the pure Fermi-Dirac distribution is plotted for comparison [15].

In the case of a prompt explosion scenario, the neutronization burst occur when the shock crosses the ν_e neutrinosphere a few milliseconds after the bounce. In the delayed scenario the shock stalls at a 100-300 km radius, beyond the neutrinospheres, leaving behind a temperature of 1.5 MeV and a density of 10^8 g/cm^3. Models predict that if a fraction between 5 and 10% of the neutrino flux is captured, the shock can be revived eventually producing the SN explosion. This mechanism would be clearly dominated by the CC cross section of ν_e and $\overline{\nu}_e$ on the free nucleons. Also, the matter falling through the stalled shock in the accretion phase can contribute to the heating of nucleons and photons, leading to an increase of the thermal neutrino flux and resulting in a luminosity hump on the low energy part of the spectrum (while the shock is still opaque to neutrinos at higher energies).

It should be noted that several numerical models used to predict the neutrino emission fail to reproduce the actual supernova explosion. This is especially true for the simpler one-dimensional models based on the spherical symmetry of the star, unless special corrections to the neutrino flux are taken into account. Multidimensional models which can simulate also convection motions are more successful but also more computationally demanding and in general strong efforts to produce more accurate simulations are still underway [6].

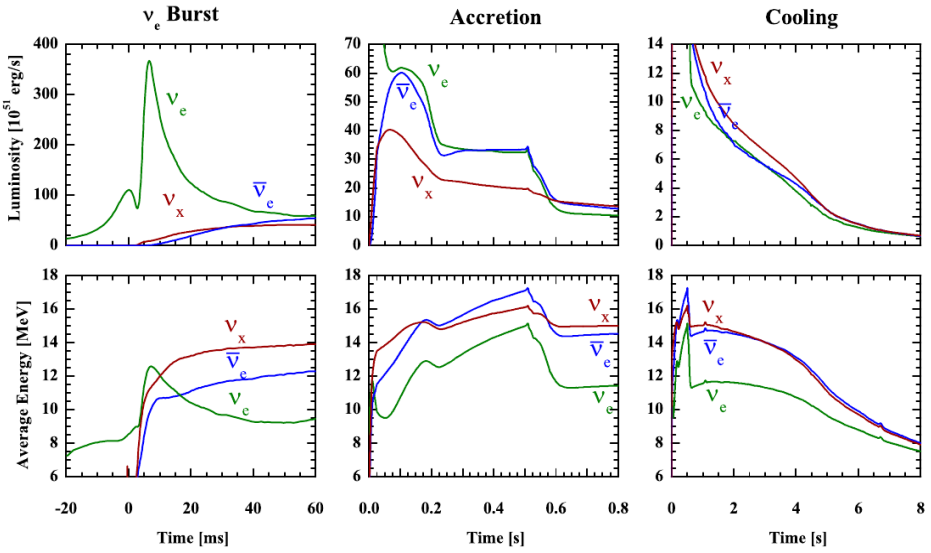

Figure 1.5: Neutrino emission phases for a core-collapse supernova, the *capture* phase is included in the first window as it occurs for a brief time before the breakout burst [11].

1.5 SN1987A

The supernova SN1987A, discovered on 24/02/1987 is the last supernova observed on Earth and the first and only supernova for which a neutrino signature has been recorded and for which the progenitor star is known.

SN1987A originated by the collapse of the blue supergiant *Sanduleak* located at a 50 kpc distance from the solar system in the Large Magellanic Cloud [16], a satellite galaxy of the Milky Way. The supernova showed a luminosity increase over the first three months with a relatively faint emission, due to the compactness of the progenitor ($R \sim 10^7$ km). Under these circumstances most of the energy is consumed in the expansion process, while the luminosity increase is due to the growing contribution of the radioactive decay of heavy elements in the inner shells, becoming more visible along the evolution. No compact remnant has been identified however there are some hints of the existence of an optical pulsar with a period of 2.14 ms [17].

The observation of the neutrino signature of SN1987A marks the starting point of extrasolar neutrino astronomy. Two water Cherenkov detectors (Kamiokande II, IMB) and two scintillation detectors (Baksan and LSD) recorded an anomalous set of neutrino interactions in the order of 10 Mev over a 10 s time window, a few hours before the optical discovery [18]. Since no proper SN trigger was in place, the events were found in the data only in the later analysis, however there are some consistency issues in the data

set. First, the LSD events were recorded approximately five hours before the other detectors, so their correlation with the supernova, although advocated by some studies [19], is disputed and they are usually excluded in combined analyses. Second, Kamiokande II events (a total of 16) are subject to a time uncertainty of about one minute due to a shift in the clock system discovered after the data analysis. A power fault at the facility prevented the synchronization of the Kamiokande II clock to a precision global time reference, so the uncertainty could not be significantly reduced [20]. No information on the incoming direction if the neutrinos can be extracted from these data as the emission of the detection processes is mostly isotropical.

SN1987A produced an estimated of 3×10^{57} ν_e releasing 3×10^{53} erg of binding energy. An estimated number of 10^{28} neutrinos has crossed the Earth yielding two dozens of observed events. The observation, even if statistically poor, is consistent with the standard model of core-collapse supernova with a strong indication for the delayed explosion scenario. The 15 MeV average energy is consistent with a cooling model of the proton-neutron star given an accretion interval of 0.7 s and a cooling time scale of about 4 s [21].

1.6 Neutrino astrophysics

Since the neutrino emission is strongly tied to the supernova evolution over the several stages, the observation of a high-statistics neutrino supernova burst with the current and planned detectors may bring unprecedented improvements on the comprehension of SN mechanics and neutrino properties.

1.6.1 Flavor conversion and mass hierarchy

Neutrinos in matter are subject to a resonant flavor conversion mechanism known as Mikheev-Smirnov-Wolfenstein (MSW) effect. In a two-neutrino mixing model, the resonance can be expressed as a function of electron density (n_e), the mixing angle (θ) and energy (E) as follows:

$$\sqrt{2} G_F n_e = \pm(\Delta m^2 \cos 2\theta / 2E) \tag{1.1}$$

where G_F is the Fermi coupling constant and the sign is positive for neutrinos and negative for antineutrinos. The efficiency (adiabaticity) of the conversion process depends also upon the Δm^2 and the smoothness of the n_e profile [22].

Two MSW resonance can take place in a core-collapse respectively determined by $(\theta_{13}, \Delta m^2_{13})$ and $(\theta_{12}, \Delta m^2_{12})$, named named high (H) and low (L) after the density levels at which they occur. The third resonance $(\mu - \tau)$, taking place at a higher density, has small observable effects. In the supernova density profile, the crossing of the L-resonance region is adiabatic,

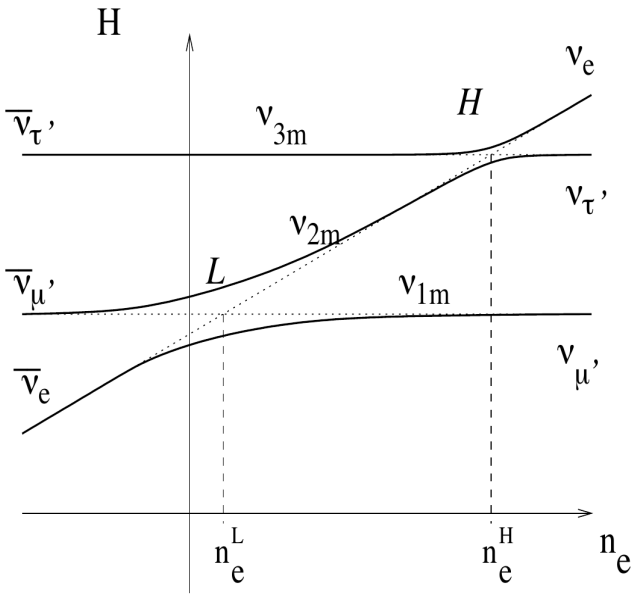

Figure 1.6: MSW effect in a supernova: evolution of the matter eigenvalues as a function of the electron number density. [11]

while the conversion in the H-resonance embodies information on the mass hierarchy that could be conveyed in the neutrino signal. The presence of shock waves and turbulence can create multiple zones where the resonance condition is met or break the adiabaticity conditions for the H-resonance [23].

It is known from recent studies that neutral current $\nu - \nu$ interactions can produce flavor conversion with a mechanism of different nature with respect to the MSW effect. The coherent $\nu - \nu$ forward scattering produces phenomena of collective pair conversion $\nu_e - \nu_e \leftrightarrow \nu_x - \nu_x$ on the full energy range even for small mixing angles. While the MSW effect arises at a radius between 10^4 km and 10^5 km, the conversion from the $\nu - \nu$ takes place deeper at 10^3 km. The occurrence of these effect is strongly dependent both on the primary neutrino spectra and on the neutrino mass hierarchy, in particular it could lead to observable alterations of the spectra only in the case of inverted hierarchy [24].

1.6.2 Neutrino mass

Due to the time dispersion given by the different propagation velocities of neutrinos of the same mass at difference energies, a neutrino burst with intrinsic duration ΔT_0 will be observed over an interval $\Delta T_{obs} > \Delta T_0$, and

this time spread can be used to put a constraint on the mass. The current model-independent mass limit on electron antineutrinos (neglecting mixing effects) is calculated to be $m_{\nu_e} \lesssim 30\,\mathrm{eV}$ [25], while with model-dependent assumptions the sensitivity can be improved to $m_{\nu_e} < 5.7\,\mathrm{eV}$ at the 95% CL [21]. The limit can be assumed valid also for the other neutrino flavors, since the known mass differences are in the order of $10^{-3}\,\mathrm{eV}$. Measurements on future SN event by SuperKamiokande could push this limit down to the 1.8-3 eV range thanks to the greater statistics. On the other hand, experiments based on the tritium decay already provide an upper limit around 2 eV for the electron neutrino mass, and the planned KATRIN experiment will outperform any limit that could be set by the SN observation. SN events could be used to constrain the masses of muon and tau neutrinos with an analysis based on the flavor-independent NC interactions [6].

1.6.3 Neutrino mixing

Hypotheses of the existence of heavier sterile neutrinos have been formulated to explain some experimental anomalies in the neutrino oscillations experiments at reactors and accelerators. In the case of a SN neutrino burst, the mixing of the electron antineutrino with a heavy massive neutrino ν_h through a matrix element U_{eh} would result in events interacting at the detector at later times with respect to the main burst. The silent time after the burst can be used to constrain both m_h and $|U_{eh}|^2$, but not independently. If the mixing angle is small (as we expect from the size of the oscillation anomalies) a very low background rate is required. The only detector able to provide data suitable for this kind of analysis on SN1987A is IMB, where no further event has been detected in the 3.9 hours after the burst. The estimate has to assume a lower limit on the mixing matrix element to evaluate the significance of the lack of events: a burst of 8 events could be followed by a heavier neutrino interaction if $|U_{eh}|^2 \gtrsim 1/8$. Under this condition and with a model-independent estimate, the mass of the hypothetical heavier neutrino can be constrained further to $m_h \gtrsim 1.1\,\mathrm{keV}$ [6] [21].

1.6.4 CP violation

The study of violations of the CP symmetry in neutrino interactions could be crucial to the understanding of the matter-antimatter asymmetry in our universe. While it has been observed in hadronic matter, the existence of violations of the CP symmetry in neutrino interactions is still disputed and under study; this holds true also for their influence on supernova dynamics. Some models predict a deviation from the standard fluxes of a few percents when taking in account effects beyond the Standard Model [26]. A high-statistics measurement of a SN burst could be used to put several constraints on these effects.

1.7 Supernova Early Warning

The current neutrino experiments participate in an network named SuperNova Early Warning System (SNEWS), aiming to provide astronomers with an early alert information about new supernova explosions: SuperKamiokande, LVD, IceCube and Borexino are currently part of the network [27].

In order to generate an alert, the system has tight coincidence requirements constraining false positives to no more of one per century. The early warning can also be used as an input trigger for experiments without self-trigger capability in case of a SN event (like noisier neutrino detectors or gravitational waves detectors).

The SNEWS system could also detect the neutrino emission from the pre-supernova phase of a massive star (over 20 $M_{\odot}$) as long as the source is within 1 kpc to ensure a sufficient signal to noise ratio over the neutrino backgrounds.

Chapter 2

SN neutrino detection in liquid scintillator

2.1 Neutrino flux model

The neutrino flux emitted by the SN is a pinched thermal distribution [28]:

$$\Phi_i = \frac{\mathcal{E}_i}{4\pi D^2} \times \frac{E^\alpha e^{-E/T_i}}{T_i^{\alpha+2}\Gamma(\alpha+2)} \tag{2.1}$$

where i refers to the neutrino species and $\mathcal{E}_i$ the total radiated energy for each species, $T_i = \langle E_i \rangle / (\alpha + 1)$ the effective temperature, being E_i the average energy and α the pinching parameter.

The choice of temperatures is far from being univocal, but several theoretical and experimental constraints exists. Combining results of theoretical simulations and best fit parameters on SN1987A electron antineutrino events from Baksan, Kamiokande II and IMB detectors a value of $\langle E_{\overline{\nu}_e} \rangle = 12\,\mathrm{MeV}$ has been estimated [29]. There are no existing experimental data from non-electronic neutrino species, but the ratio between $\langle E_{\nu_x} \rangle$ and $\langle E_{\overline{\nu}_e} \rangle$ can be estimated through the core cooldown model, as we know that the lower cross sections result in a hotter emission radiating from a smaller neutrinosphere. The value of $\langle E_{\nu_x} \rangle$ can be set between $\langle E_{\overline{\nu}_e} \rangle$ and 15.6 MeV ($\sim 30\%$ hotter) according to existing theoretical simulations [30]. A similar approach can be used to estimate the temperature of the electron neutrinos emission, taking in account its dependence on the proton fraction of the star, given by the charged-current interactions. For a typical proton fraction of 0.4 we can assume $\langle E_{\nu_e} \rangle = 9.5\,\mathrm{MeV}$.

2.1.1 Survival probability

As we have examined in the previous chapter, there are two neutrino flavor conversion phenomena taking place inside the core as the neutrinos propagates to the surface. The neutrino fluxes radiating from the neutrinosphere

are thus subject to changes in their composition depending both on the core density profile and on the neutrino mass hierarchy. An up-to-date derivation of the neutrino fluxes at the Earth can be found on reference [24], here we summarize the resulting survival probabilities for ν_e and $\overline{\nu}_e$ which are highly sensitive to the the mass hierarchy [29]:

Survival probability	**Normal**	**Inverted**
$\overline{\nu}_e \to \overline{\nu}_e$	0.7	0.0
$\nu_e \to \nu_e$	0.0	0.3

We can see first that the detection of electron antineutrinos is more or less suppressed in both the scenarios, second that in the case of inverted hierarchy all the electron antineutrinos detected on the Earth are of non-electronic flavor at the source, with a significant loss of the information that could be carried by the electronic channel.

2.1.2 Flux dataset

We based our analysis on the *Supernova Neutrino Database* data [31] provided by a 2013 study combining neutrino radiation hydrodynamic for the early phase and quasi-static neutrino diffusion for the late phase of the supernova. We have chosen a typical model with initial mass of 30 $M_\odot$, $Z = 0.02$ metallicity and a revival time of 300 ms: in agreement with the existing literature the flux yields $\sim 5 \times 10^3$ IBD events for a 20 kton detector.

We have chosen to examine only the case of the normal neutrino mass hierarchy.

We hereby show the time and energy spectra of the post-oscillation flux expected at the detector for a 10 kpc supernova: we remind that in case of nearer or farther sources no change in the oscillation pattern are expected, so all the rates can be rescaled as a function of the distance only.

Energy and time spectra of the neutrino flux are shown in figures 2.1 and 2.2, the time scale is such that the onset of the collapse takes place at 50 ms. It is important to notice that in the early phase of the core collapse the non electronic component of the neutrino flux, that can be detected only via NC processes, dominates on the others.

2.2 Detection channels

Several interaction channels are available in a scintillation detector. The main detection process is the *inverse beta decay* (IBD). Other processes include NC and CC interactions with nuclei and elastic scattering on protons and electrons. CC processes provide a direct signature of the incoming neutrino flavor and energy - which are mirrored by the produced lepton - but at these energies CC interactions are available only for the electronic

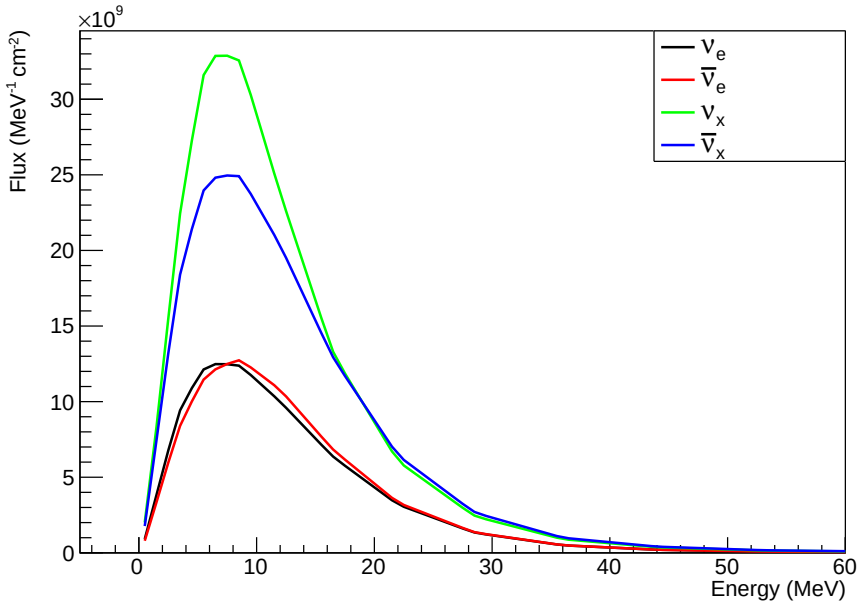

Figure 2.1: Fluence of a 10 kpc SN neutrino burst.

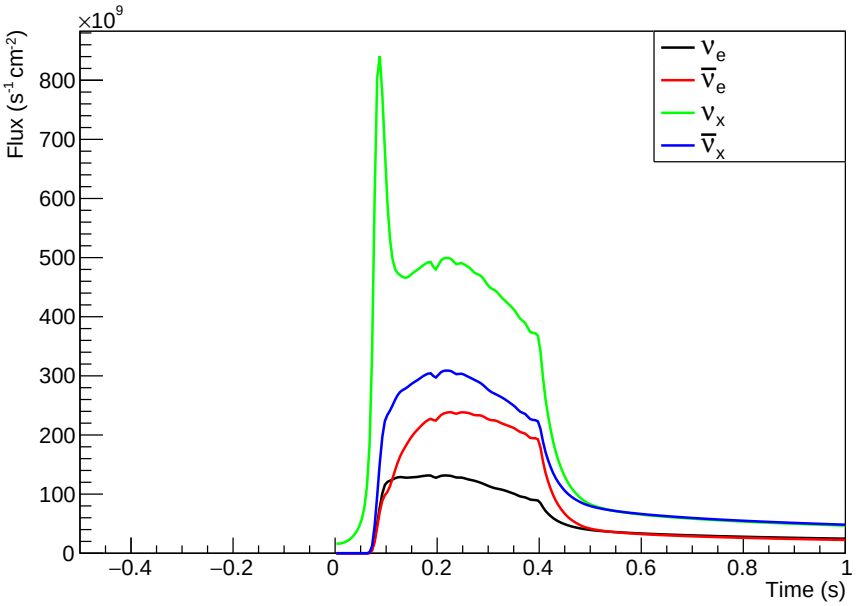

Figure 2.2: Time spectrum of the flux for a 10 kpc SN neutrino burst.

species. NC processes do not allow for the reconstruction of the single neutrino energy, but some information on the incoming spectrum can be statistically inferred: knowing the process threshold and the dependence of the cross section on the energy it is possible with a best-fit strategy to estimate the spectrum parameters which are in agreement with the number of observed events.

We will here estimate the interaction rates according to the cross section plotted in figure 2.3 for a generic 20 kton scintillator detector, accounting for the same fiducial mass of the JUNO detector, that we will introduce in the next chapter.

Process	Formula	Type	Threshold
Inverse beta decay (IBD)	$\overline{\nu}_e + p \rightarrow n + e^+$	CC	1.8 MeV
Proton elastic scattering	$\overset{(-)}{\nu} + p \rightarrow \overset{(-)}{\nu} + p$	NC	-
Electron elastic scattering	$\overset{(-)}{\nu} + p \rightarrow \overset{(-)}{\nu} + p$	NC + CC	-
Superallowed ^{12}C	$\nu + {}^{12}\mathrm{C} \rightarrow \nu + {}^{12}\mathrm{C}^* \rightarrow \nu + {}^{12}\mathrm{C} + \gamma$	NC	15.1 MeV
Superallowed CC	$\nu_e + {}^{12}\mathrm{C} \rightarrow {}^{12}\mathrm{N} + e^-$	CC	17.3 MeV
Superallowed CC	$\overline{\nu}_e + {}^{12}\mathrm{C} \rightarrow {}^{12}\mathrm{B} + e^+$	CC	14.4 MeV

Table 2.1: Summary of neutrino interaction channels in liquid scintillator

At the SN neutrino energy scale, CC and NC interactions on nuclei are still poorly understood from a theoretical point of view, resulting in large uncertainties in the order of 10-20% on the values of the estimated cross sections. A more accurate knowledge of the cross sections from theoretical calculations and experimental constraints from planned experiments could provide a great advantage in the analysis of a future supernova event. We will use the cross sections shown in figure 2.3.

2.2.1 Inverse Beta Decay

The main antineutrino detection process in a liquid hydrocarbon-based scintillator detector is the *inverse beta decay* (IBD) for electronic antineutrinos:

$$\overline{\nu}_e + p \rightarrow n + e^+ \tag{2.2}$$

The positron mass added to the mass difference between the neutron and the proton result in a kinematic threshold of 1.8 MeV. After the interaction, the positron releases its energy and annihilates with an electron, while the neutron scatters, thermalizes and gets captured on a free proton. The reaction produces a deuteron and a 2.2 MeV photon. The neutron capture time has an exponential distribution with an average of $\tau \simeq 250\,\mu$s. The observable signature of a IBD event is the combination of a *prompt* signal

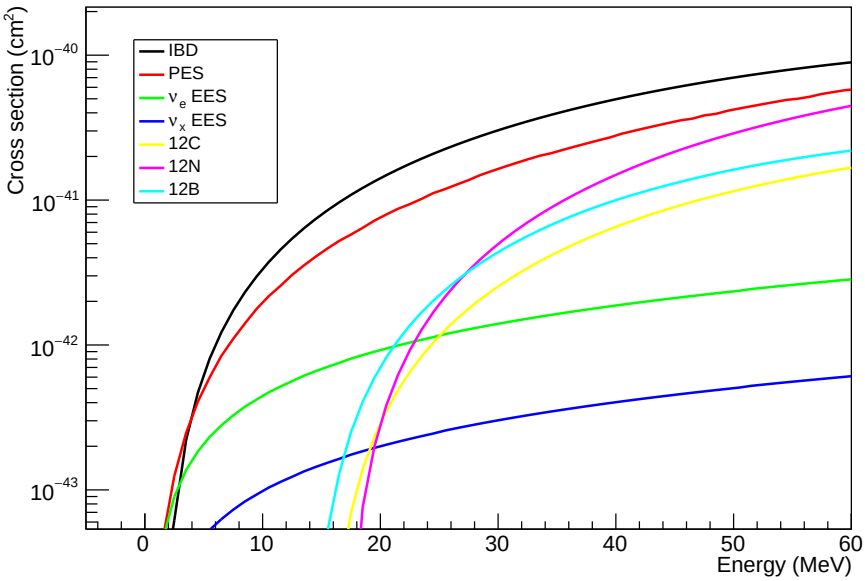

Figure 2.3: Neutrino interaction cross sections in liquid scintillator

given by the positron energy release and a *delayed* signal from the neutron capture, separated by a time interval with distribution:

$$f(\Delta t) = \tau^{-1} e^{-\frac{\Delta t}{\tau}} \tag{2.3}$$

As seen in figure 2.4 the detected positron energy has a continuous spectrum that mirrors the neutrino energy spectrum through the following kinematic balance (given a Q-value for the process of $Q \simeq 1.3\,\mathrm{MeV}$ and the electron mass $m_e \simeq 0.5\,\mathrm{MeV}$):

$$E_\nu = (E_d - m_e) + Q = E_d + 0.7\,\mathrm{MeV} \tag{2.4}$$

Neutron capture photons are mainly detected through Compton scattering on the scintillator molecules with a spectral shape determined by the scintillator quenching effects. The scintillator can be doped with gadolinium resulting in a higher cross section for neutron capture (dominating by several order of magnitudes on free protons) and a stronger capture gamma emission of 8 MeV. However, as the doping significantly reduces the transparency of the medium, this option is unsuitable for very large scintillator detectors.

While the positron is emitted almost isotropically in a IBD interaction, the neutron is produced with a forward distribution that can be exploited to find the incoming neutrino flux direction when enough statistics is provided.

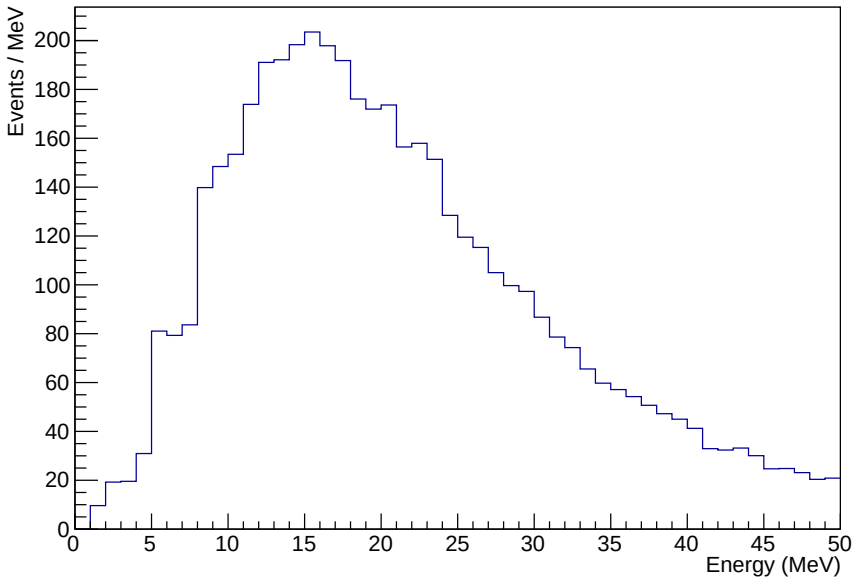

Figure 2.4: Positron energy spectrum for a 10 kpc SN neutrino burst at a 20 kton liquid scintillator detector.

Inverse beta decay events can be tagged by searching for a neutron capture signal within a 1 m radius [32] and within a time interval $T = 2\tau \simeq 500\,\mu$s with reference to the prompt emission vertex. The tag is possible as long as the number of events inside the time window and the specified volume does not exceed the unity:

$$R_{IBD} \cdot \Delta t \cdot \left(\frac{\Delta V}{V_{DET}} \right) \leq 1 \tag{2.5}$$

We can therefore put a lower limit on the SN distance that allows the full disentangling of the single IBD events: first, we calculate the peak interaction rate as a function of the distance with the plot in figure 2.5.

From the time spectrum shown in fig. 2.5 for a 10 kpc supernova we have a peak rate of ~ 200 events per 20 ms between 300 and 400 ms, equivalent to ~ 100 kHz. From this reference point we can estimate the rate as a function of the distance (in kpc) as follows:

$$R_{IBD} = 10^5 \cdot \left(\frac{10}{D} \right)^2 Hz \tag{2.6}$$

Combining equations 2.6 and 2.5 we can put a lower limit of $D \simeq 1$ kpc for the full theoretical IBD tagging capability.

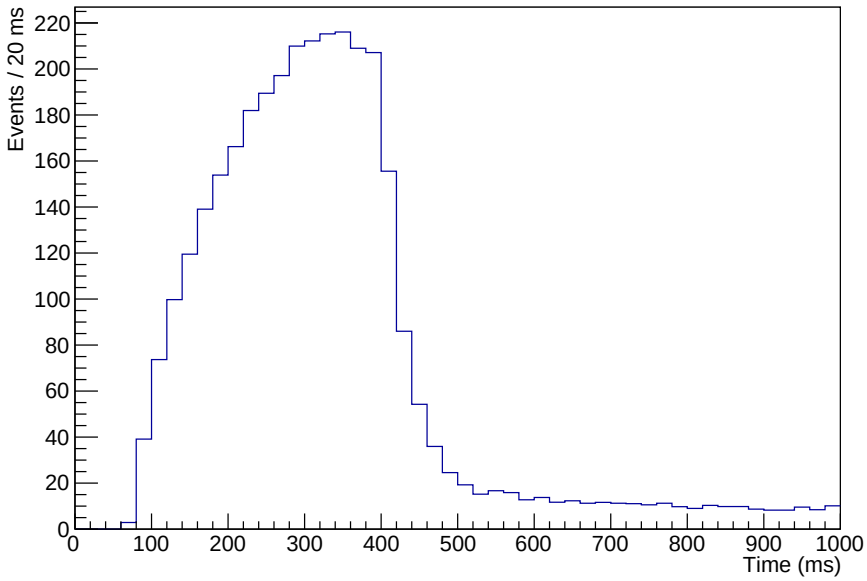

Figure 2.5: Positron time spectrum from inverse beta decay interactions for a 10 kpc SN burst at a 20 kton liquid scintillator detector.

2.2.2 Elastic scattering

Coherent elastic scattering on protons and nuclei through NC interactions is expected to occur at a high rate, however the recoil energy of nuclei is too low to be detectable, so only electrons and protons (from hydrogen) are of interest. Elastic scattering cross sections can be seen in fig. 2.3.

Protons

The experimental cross section for this channel is known with an uncertainty of about 17% due to the poor existing experimental statistics, while the theoretical estimates have a 20% uncertainty due to the fact that precision QCD calculations accounting for the internal structure of the proton are difficult. The neutrino-proton elastic scattering can be summarized as follows:

$$\overset{(-)}{\nu} + p \rightarrow \overset{(-)}{\nu} + p \tag{2.7}$$

The light signal is given by the recoil energy of the proton, which is low due to its relatively high mass. This process yields a large number of events at the low end of the energy spectrum, with a distribution sharply decaying

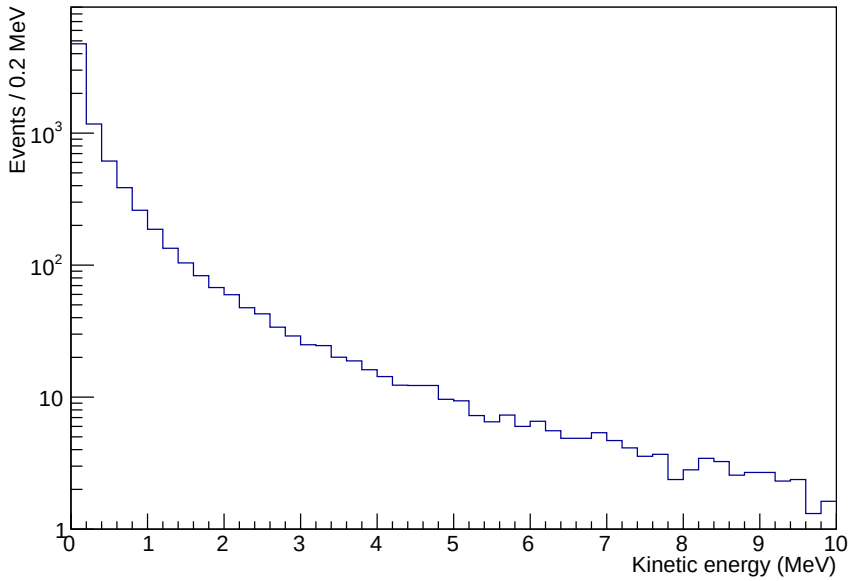

Figure 2.6: Proton kinetic energy spectrum produced in ES for 10 kpc SN burst at a 20 kton liquid scintillator detector.

within a few MeVs as shown in figure 2.6. The effective number of detected events has a strong dependence on the PMT system detection threshold.

The protons in the scintillator are subject to quenching effects resulting in a reduced light output with respect to the original recoil kinetic energy T_p, depending on the chemical composition of the scintillator. The visible energy can be parametrized as follows:

$$E_d = a_1(1 - e^{a_2 + a_3 \cdot T_p}) \cdot T_p$$

where the a_i are fitting parameters. The quenching combined with the scintillation process threshold set a minimum kinetic energy for the detection of the proton recoil, which in turn determines a minimum energy for the neutrino to be detected even if the process has no kinematic threshold. This makes this channel unsuitable for the exploration of the lower part of the neutrino spectrum.

Electrons

The elastic scattering process on electrons is expressed as follows:

$$\overset{(-)}{\nu} + e \rightarrow \overset{(-)}{\nu} + e \tag{2.8}$$

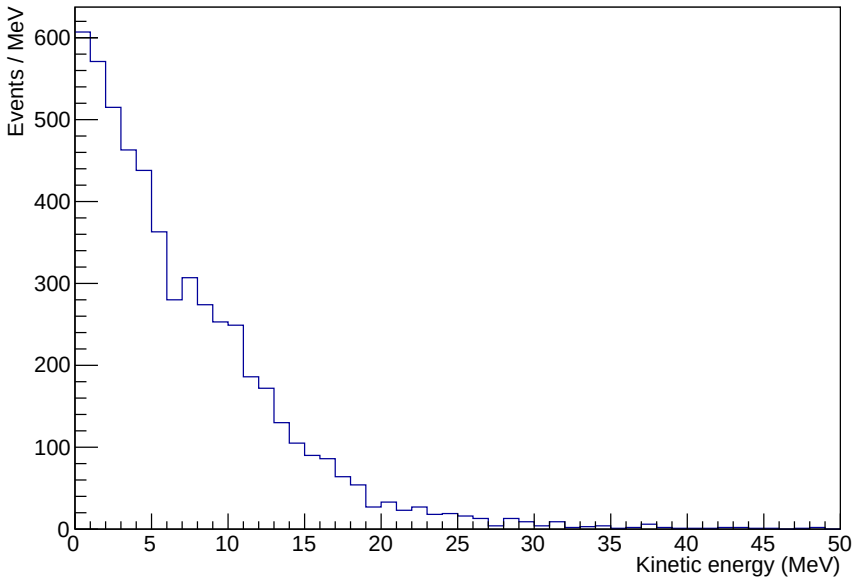

Figure 2.7: Electron kinetic energy spectrum produced in ES for 10 kpc SN burst at a 20 kton liquid scintillator detector.

Both charged current from electron flavors and neutral current from any flavor participate in the process cross section, that can be parametrized as follows [30]:

$$\sigma = \frac{1}{2}(\sigma_\nu + \sigma_{\overline{\nu}}) = G_F^2 E_\nu^2 \cdot 10^{q(E_\nu)} \tag{2.9}$$

where G_F is the usual Fermi coupling constant and $q(E_\nu)$ is a fitting function in the form of $q(E_\nu) = -0.333 - 0.16(E_\nu 100\,\mathrm{MeV})$. The resulting spectrum is shown in figure 2.7.

2.2.3 Superallowed NC interaction

The *superallowed NC reaction* on ^{12}C produces a 15.11 MeV de-excitation photon:

$$\nu + {}^{12}\mathrm{C} \rightarrow \nu + {}^{12}\mathrm{C}^* \rightarrow \nu + {}^{12}\mathrm{C} + \gamma \tag{2.10}$$

The cross section for this process below 100 MeV can be expressed as [30]:

$$\sigma = \frac{1}{2}(\sigma_\nu + \sigma_{\overline{\nu}}) = \frac{G_F^2 E^2}{\pi}(E - 15.11\,\mathrm{MeV})^2 \cdot 10^{p(E)} \tag{2.11}$$

where $p(E) = \sum_{n=0}^{3} c_n (E/100\,\mathrm{MeV})^n$ is a function of the incoming neutrino energy and four numerical coefficients c_n. The tagging of superallowed NC

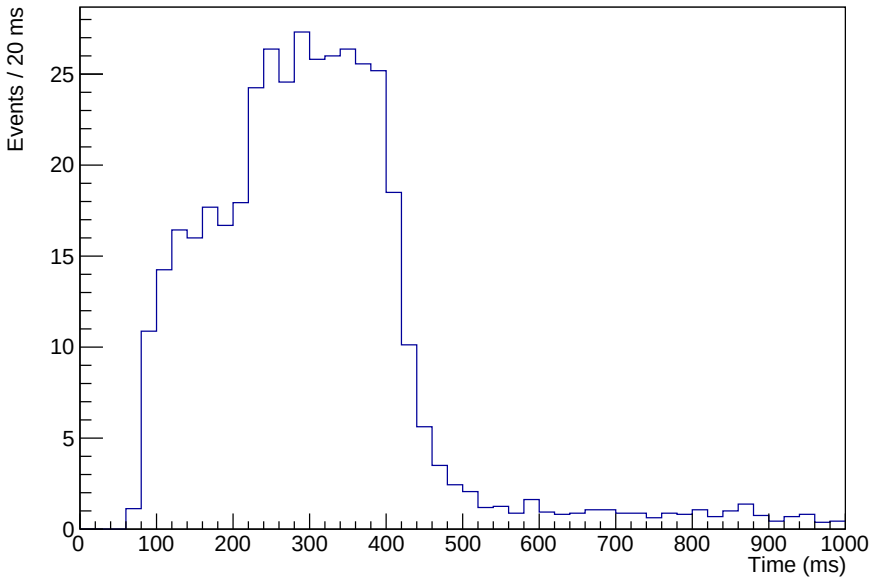

Figure 2.8: Superallowed NC time spectrum for a 10 kpc SN burst at a 20 kton liquid scintillator detector.

events is purely based on the statistical discrimination with a cut on the energy spectrum around the center value of 15.11 MeV. As the ^{12}C interaction is purely neutral current, its rate shown in fig. 2.8 provides a good measurement of the total SN neutrino emission.

2.2.4 Superallowed CC interactions

Only ν_e and $\overline{\nu}_e$ charged current interactions are allowed at the energy scale of SN neutrinos, as the energy is under the thresholds for the production of heavier leptons. The *superallowed CC reactions*:

$$\nu_e + {}^{12}\mathrm{C} \rightarrow {}^{12}\mathrm{N} + e^- \quad (E_{\nu_e} > 17.3\,\mathrm{MeV}) \tag{2.12}$$

$$\overline{\nu}_e + {}^{12}\mathrm{C} \rightarrow {}^{12}\mathrm{B} + e^+ \quad (E_{\overline{\nu}_e} > 14.4\,\mathrm{MeV}) \tag{2.13}$$

result in a continuous spectrum given by the prompt energy release of the electron (resp. positron) followed by β^+ (resp. β^-) decay of ^{12}N (resp. ^{12}B) to ^{12}C, with half-life of 11 ms (resp. 20 ms). The spectra are shown in figures 2.9 and 2.10. The delayed emission could in principle be used to tag the event, but the decay time window is very large if compared to the SN burst interaction rates and the beta decay spectrum could be shadowed by the electron elastic scattering interactions. A proper strategy needs to be put in place in order to disentangle this channels.

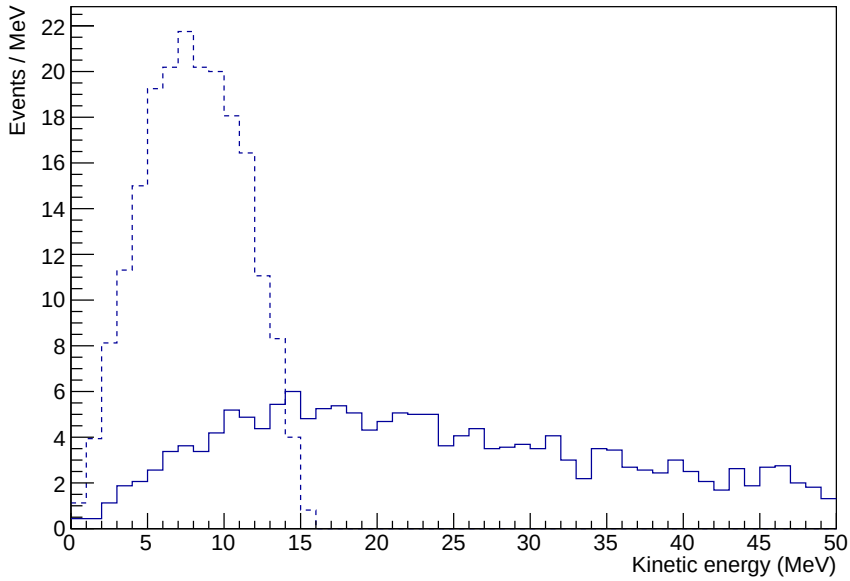

Figure 2.9: Superallowed CC ^{12}N, positron (solid) and beta decay electron (dashed) for a 10 kpc SN burst at a 20 kton liquid scintillator detector.

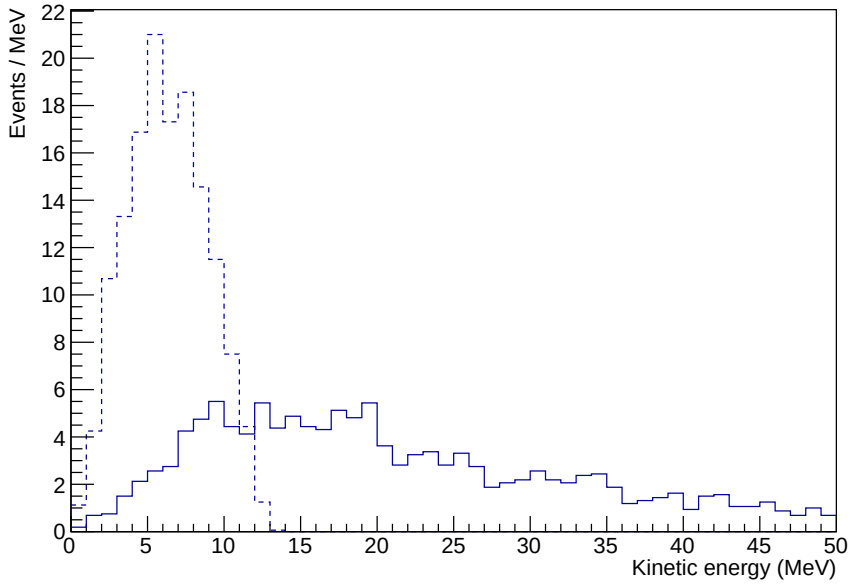

Figure 2.10: Superallowed CC ^{12}B, electron (solid) and beta decay positron (dashed) for a 10 kpc SN burst at a 20 kton liquid scintillator detector.

Chapter 3

JUNO scintillation detector

The Jiangmen Underground Neutrino Observatory (JUNO) is a multipurpose underground neutrino detector planned for construction in the Jiangmen region of China. JUNO's main purpose is the observation of nuclear reactor antineutrinos from the Yianjang and Tiashan nuclear power plants on a baseline of $\sim$ 50 km, aimed to determine the still unknown neutrino mass hierarchy. Following BOREXINO and KamLAND it will be the largest liquid scintillator experiment ever built.

An extensive description of the JUNO detector can be found in the JUNO Conceptual Design Report [33] while the physics capabilities are reviewed in the JUNO Yellow Book [34].

The detector is a spherical acrylic vessel of 35.5 m diameter filled with 20 kton of high transparency liquid scintillator. The photomultiplier configuration has been determined as $\sim$ 18000 large (20") PMTs and $\sim$ 34000 small (3") PMTs. The total optical coverage is 80% and the expected energy resolution is $\frac{3\%}{\sqrt{E}}$. The sphere will be shielded by a water buffer provided with $\sim$ 1500 PMTs to detect the Cherenkov emission and a muon top tracker based on the plastic scintillators already used in the OPERA experiment [35].

The target energy resolution, given by the Poisson statistics, requires the detection of 1200 photoelectrons per MeV. This number depends on the light yield and the attenuation length of the scintillator plus the optical coverage and the efficiency of the photomultipliers.

3.1 Liquid scintillator

The active volume of the detector is made by 20 000 ton of liquid scintillator, an hydrocarbon with benzene rings that is subject to excitation and subsequent light emission on a wavelength between the blue and near-UV part of the spectrum.

The composition of the scintillator material is actually a solution of dif-

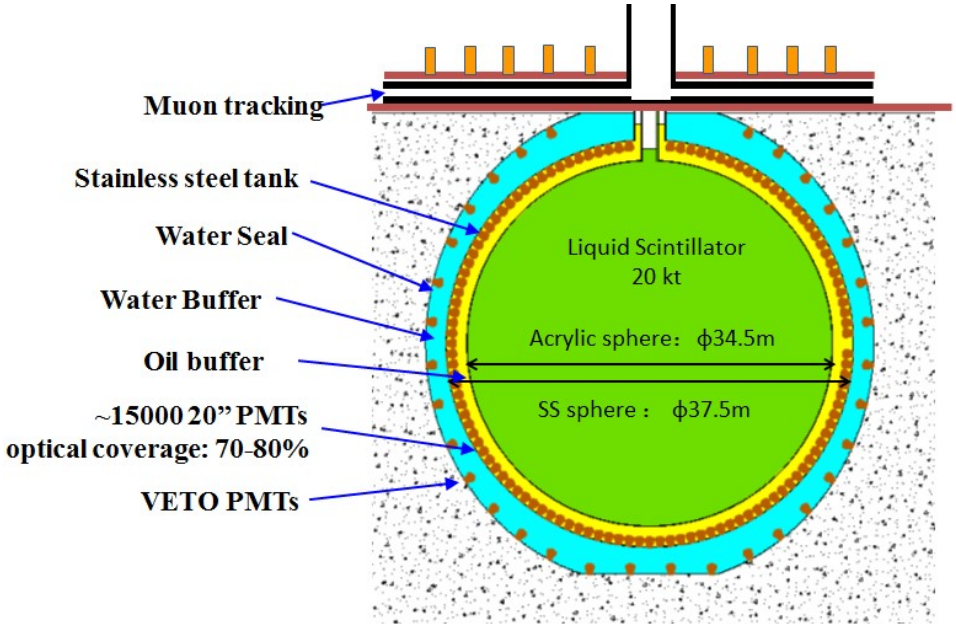

Figure 3.1: Basic diagram of the JUNO detector

ferent substances with different purposes: the bulk of the target material is linear-alkyl-benzene (LAB) in which a fluor (PPO) and a wavelength shifter (Bis-MSB) are dissolved in low concentrations (resp. 3 g/l and 15 mg/l). The interaction between the LAB and the other two components produces a conversion of the light wavelength to $\sim$ 430 nm, necessary to avoid the self-absorption by the LAB excitation modes. At this wavelength, the transparency of the media is mainly dependent on the Rayleigh scattering.

Transparency requirements are of a minimum attenuation length of 22 m at 430 nm and an absorption coefficient under 3×10^{-3} over the full spectral range between 300 nm and 600 nm.

3.1.1 Signal time profile

The scintillation light is emitted within 20 ns from the interaction, while the propagation time of the photons inside the detector accounts for a time spread up to 500 ns in the PMT hits. The scattering photons that may be produced could also hit the PMTs at later times with respect to this interval. In the offline event reconstruction the arrival time of each hit can be corrected once the vertex position has been reconstructed, however as the information is not available in real-time for trigger purposes one must define an acquisition window including the full spread in order to acquire the large PMTs signal. The small PMTs are self-triggered, but the same

time window can be used to define the identification of a signal based on the hit coincidences.

The time profile of the emission has a slight dependence on the type of the interacting particle, so electrons and protons could in principle be identified by means of *pulse shape discrimination* [34].

3.2 Photomultiplier configuration

In January 2016 JUNO took the final decision for the procurement of the large PMT detectors. Two options were available: the Hamamatsu R12860 PMT, the same used by SuperKamiokande experiment, and one of new development by the North Night Vision Technology[1] which uses multi channel plate (MCP) instead of conventional discrete dynodes. The characteristics of the two PMTs are summarised in table 3.1. After an optimization based on cost and performance of the two options, JUNO decided to use 13000 MCP-PMT and 5000 Hamamatsu PMT.

Table 3.1: JUNO large PMTs characteristics

Characteristics	MCP PMT	R12860
Quantum Efficiency at 400 nm (%)	26 (Tested), 30 (R&D)	30
Single Photo-electron (P/V)	3+	3+
Transient Time Spread (ns)	12	3
Rise Time - Fall Time (ns)	~ 2, ~ 10	~ 7, ~ 17
Anod Dark Count (Hz)	30 k	30 k
After Pulse (%)	3	10
Glass	Low-Potassium Glass	Hario-32

The $3''$ PMTs are located in the gaps between the large PMTs and their number is roughly 2:1 with respect to large PMTs. Figure 3.2 show the large and small photomultiplier arrangement structure. The total optical coverage of the small PMTs is about 4% and the mean number of photons hitting a $3''$ PMT is about 0.01 per MeV of deposit energy at the center of the detector. This implies that the small PMTs will be hit most of the time by no more than one photon and the energy deposit can be reconstructed by simply counting the number of $3''$ PMT which have been hit within the event time window. The required characteristics of the $3''$ PMT is an excellent single photon detection, high gain, and low noise. With these characteristics there are few options on the market, some also taken into account by the KM3Net collaboration [36].

[1] http://www.nvir.cn/

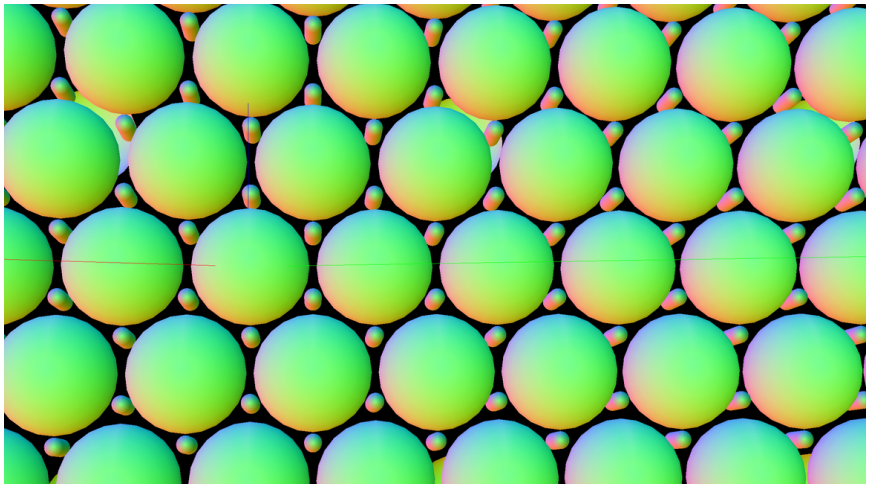

Figure 3.2: PMT arrangement in JUNO.

Figure 3.3: 3″ photomultiplier

Figure 3.4: 20″ MCP photomultiplier

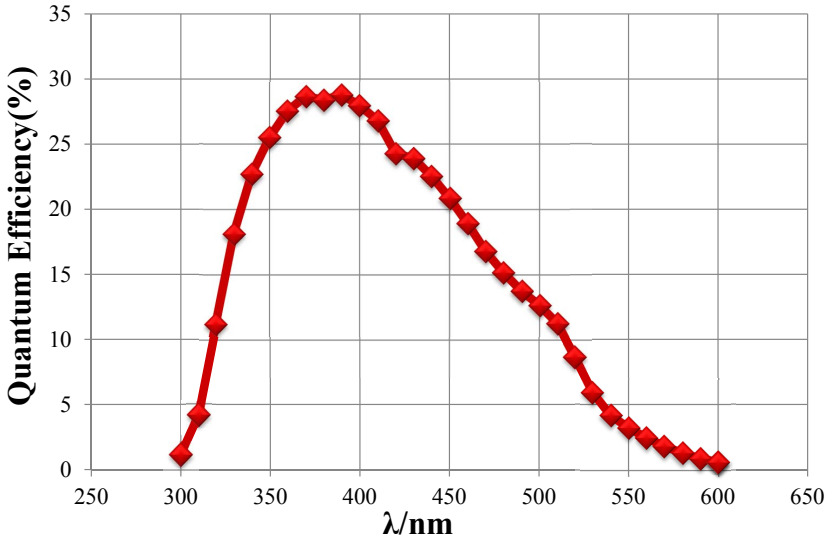

Figure 3.5: Quantum efficiency plot for the MCP photomultipliers

3.3 Readout strategies

Depending of the light level observed by the PMTs there are two readout strategies available:

Charge integration or photon counting: the total number of photons hitting the PMT is reconstructed either integrating the charge collected from the PMT over a defined time interval with a proper calibration of the readout channel or acquiring the PMT waveforms, using a sampling ADC, to reconstruct offline the pulses of the single photons hitting the PMT. In both cases the PMT calibration or the algorithm to reconstruct the single hits can introduce a bias in the energy reconstruction.

PMT counting: if the probability to have more than one photon per event hitting a PMT is low, a digital readout of the PMT output signal in a defined time interval is sufficient. In this case no calibration of the single channels is needed and the nonlinearity due to more then one photon hitting the PMT can be corrected using the Poisson statistics, as follows:

$$N_{corr} = -N_{PMT} \log\left(1 - \frac{N_{PC}}{N_{PMT}}\right) \tag{3.1}$$

Figure 3.6 shows the *illumination* λ, defined for the PMT closest to the interaction vertex as the ratio between the number of photons hitting the PMT and the total number of PMTs hit within the event. Only for the

events in the central section of the detector the illumination is low enough to allow for the energy reconstruction via both the methods. For the vast majority of the events, which occur far from the center of the detector, the illumination of the closest large PMT is very high and the PMT counting method becomes unsuitable.

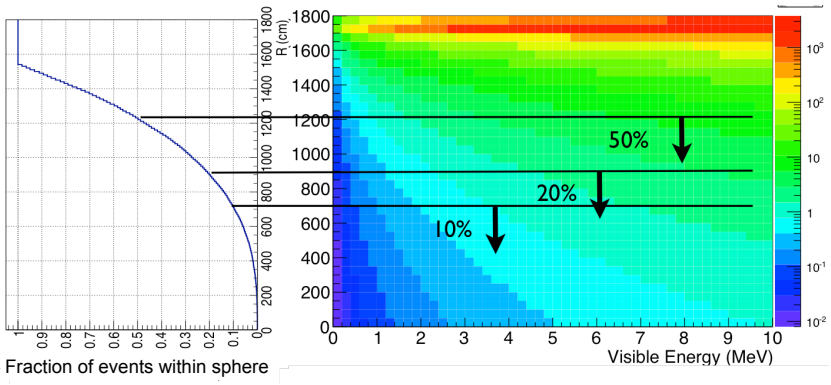

Figure 3.6: (Right) Illumination of the closest large PMT as a function of the energy deposit and position of the event. The illumination λ is defined as the ratio between the number of photons hitting a PMT and the number of hit PMTs. (Left) The fraction of IBD events within a sphere of given radius. Horizontal lines indicate the radius of a sphere containing respectively 10%, 20% and 50% of the events.

3.3.1 Readout electronics

JUNO is the first liquid scintillator detector with the readout electronics totally submerged in the water buffer. For the LPMT the front-end electronics (FEE) is mounted on the back of the PMT in a watertight box and connected to the external world by two shielded UTP CAT5e cables which are used to transmit data, trigger information and slow control signals along the distribution of the clock. The same cables are used to provide the low voltage, while the PMT high voltage is generated locally using a Cockcroft-Walton generator.

The LPMT front-end electronics (FEE) contains the local power supply board, the already mentioned high voltage power supply for the PMT anode and the *Global Control Unit* (GCU) containing the readout and acquisition system based on an ADC and a system-on-chip (SoC) computer. The FEE implementation makes each LPMT an autonomous unit with the potential for advanced on-line processing capabilities.

The SPMT front-end electronics is simpler and based on a dedicated *CatiROC* ADC unit. Each GCU implements 8 CatiROC units, each one

collecting the data from 16 SPMTs for a total of 128 SPMTs per GCU. The unit also includes 8 HV power supplies, each one feeding 16 HV lines. The signal is read directly on the anode after proper decoupling of the HV DC component.

3.3.2 Photomultiplier dark noise

Coincidence of the dark noise hits on multiple PMTs can result in fake events the vertex at the center of the detector. The result is a background noise that effectively limits the lower energy threshold achievable by the detector, however this noise can be greatly reduced offline with a proper filter on the vertex position.

For the large PMTs the detector has an energy threshold of $\sim 0.4\,\mathrm{MeV}$ due to the floor of dark noise that can be lowered to $0.1\,\mathrm{MeV}$ by means of vertex selection, losing approximately two percent in efficiency [34].

For the small SPMTs we will have to establish a trigger threshold allowing for the identification of a signal event over the dark noise background.

Chapter 4

Simulation framework

The study of a supernova event in the JUNO detector required the implementation of an appropriate simulation framework, combining a supernova Monte Carlo generator and a JUNO Monte Carlo suite for the simulation of the detector.

4.1 JUNO supernova generator

A supernova Monte Carlo generator has been developed by Yu-Feng Li and Liang-jian Wen and presented at the JUNO 6th collaboration meeting held on July 2015 at IHEP[1]. The generator takes in input a SN time-dependent neutrino flux and provides at the output the products of each interaction taking in account cross sections and event kinematics. The simulation can be adjusted for normal or inverted hierarchy and supernova distance.

4.2 JUNO detector Monte Carlo simulation

The complete JUNO Monte Carlo suite was deemed too complex and overfeatured in relation to our needs, so we based our work on a simpler but effective JUNO multi-calorimetry Monte Carlo (JMC) that has been developed by Stefano Dusini and Margherita Buizza Avanzini (École polytechnique) to evaluate the response of the detector with the introduction of the small photomultipliers setup.

The suite is based on the GEANT4 geometry and tracking simulation framework [37], providing a full event-by-event tracking for individual particles and the recording of the single photomultiplier hits.

The JMC MC code implements the scintillator light emission according to the JUNO liquid scintillator model [33]. The shape of the scintillator pulse is described as the sum of two exponential decay functions:

[1] http://juno.ihep.ac.cn/cgi-bin/Dev_DocDB/ShowDocument?docid=1318

$$n(t) = A_{fast} \exp^{-\frac{t}{\tau_{fast}}} + A_{slow} \exp^{-\frac{t}{\tau_{slow}}} \quad (4.1)$$

where the τ parameters denote the fast and slow decay time constants of the corresponding decay process and the A parameters their amplitudes. In the simulation we have used a time constant of 4.93 ns and 20.6 ns for the fast and slow de-excitation modes respectively. The amplitude of the decay process depends on the $\frac{dE}{dx}$ which in turn depends on the particle type.

4.3 Software development

Since the output of the SN generator cannot be directly fed to the JMC software, we have developed a simple processing tool to read the output data of the SN generator and encode them on a ASCII file using the HepMC event record format [38]. The program also uniformly randomizes the position of each event over the detector fiducial volume.

The JMC software has been extended to support the HepMC input file format implementing a pre-existing class available in the Geant4 libraries, since no generic file-based input was supported by default. This modification provides a standardized and simple way to feed generic event sets to the Geant4 simulation via ASCII files.

A generic event generator has also been developed for calibration purposes and is capable of generating an arbitrary number of particles with a chosen distribution for momentum and position.

The JMC software output is a ROOT file containing a TTree with the result of the event-by-event simulation. The output information relevant to our analysis is here summarized:

- MC truth for interaction vertex coordinates and event kinetic energy;
- number of hit SPMT and LPMT for each event;
- total number of hits for LPMTs and SPMTs;
- PMT identifier and global time (referenced to the event base time) for each PMT hit.

In order to aid the analysis of IBD and other two-vertices events, the JMC has been modified to provide on the output the position of second vertex and, for each PMT hit, an identifier of the primary particle from which the photon originated. This allows for a full truth-based disentangling of the prompt and delayed emission photons. In addition, since the default timestamp for the PMT hits is relative to the event base time, the latter needs to be reported on the output file to allow a proper cross-event analysis.

Chapter 5

Analysis

As we have introduced in the second chapter, we have chosen a typical supernova model with initial mass of 30 $M_{\odot}$, $Z = 0.02$ metallicity and a revival time for the shock of 300 ms. Most of analysis that follows is based on a 2.5 kpc simulation rescaled to 10 kpc, as this is the average distance of known SN progenitors. The result is equivalent to an average over 16 independent 10 kpc SN events with the same parameters.

We have then chosen to focus on the response of the small PMT system for three particular reasons: the first is that the high-rate of a SN event could blind the large PMT readout system due to the limited size of the GCU buffer, especially if the supernova is very near; the second is that the faster response and the self-triggering capability of the small PMTs could be used for the generation of a trigger for the large PMT system; the third is that at the time of the start of this work, the large PMT performance had already been extensively treated in the JUNO Yellow Book [34] while the study of the small PMT system was still in a very early stage.

5.1 Characterization of the signal

The small photomultipliers are self-triggered, meaning that every time a hit is recorded the control unit produces and sends a data packet with the PMT information and the hit timestamp. In principle all the events can be reconstructed in the offline analysis, but we are also interested in the online triggering capabilities.

We need to analyze the signal time profile in order to establish a time window in which all the PMT hits from the same interaction vertex are recorded, then a signal event can be identified if the number of hit PMTs within that time window falls over the threshold for the rejection of the photomultiplier dark noise.

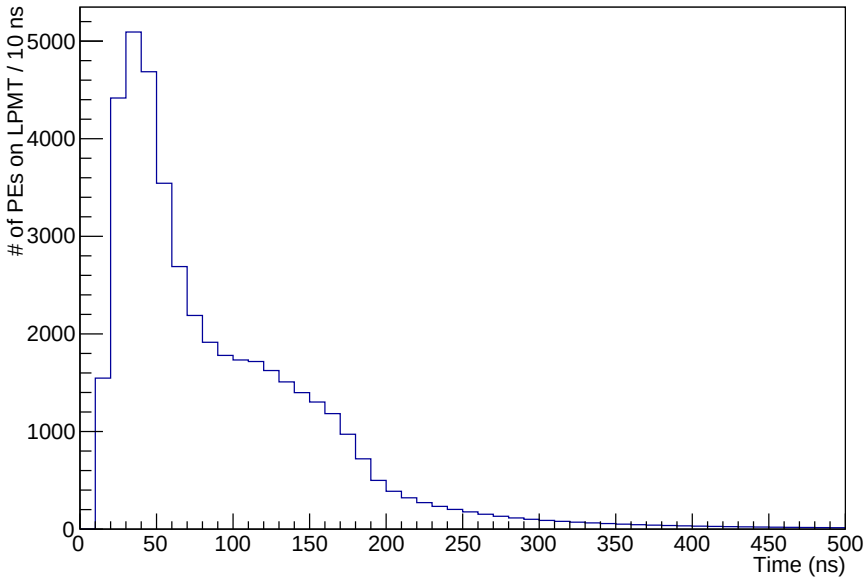

Figure 5.1: Averaged time spectrum of the PMT hits for events with vertex in the outer shell of the detector (R > 11.5 m)

5.2 Time profile of the signal

We use a sample of randomly distributed events and separated them depending on the distance of the interaction vertex from the detector center (i.e. the radius in the spherical coordinates). We expect a larger time spread for the events occurring at the edge of the detector. We divide the detector in three concentric volumes by dividing the radius in three identical segments and we select the events occurring in the outer spherical shell. The averaged time distribution of the hits can be seen in figure 5.1: all the PMT hits fall within a window of 500 ns and this will be our choice for the trigger window.

5.3 SPMT dark noise

Assuming a dark noise rate of 1 KHz for the small photomultipliers, we simulate the distribution of the random coincidences to evaluate the trigger rate given from the dark noise. We make a conservative choice by setting a threshold of 30 hit SPMT within 500 ns to select an event as signal over the dark noise background. While this background can in principle be statistically reduced in the offline analysis as its distribution is well known and the events are reconstructed at the center of the detector, this information

Table 5.1: Neutrino background rates for a supernova neutrino burst.

Type	**Rate**
Reactor neutrinos	10^{-3} Hz
Geoneutrinos	2×10^{-5} Hz
Atmospheric	$<10^{-5}$ Hz
Natural radioactivity	$<10^{-5}$ Hz
Cosmogenic isotopes	$<10^{-5}$ Hz

Table 5.2: Radioactive and cosmogenic sources background for a supernova neutrino burst.

Type	**Rate**
^{85}Kr (0.2-1 MeV)	1 Hz
^{210}Bi (0.2-1 MeV)	7 Hz
Natural radioactivity (> 0.7 MeV)	10 Hz
Cosmogenic muons	3 Hz
Cosmogenic ^{11}C	1.9×10^{-1} Hz
Cosmogenic ^{8}Li	1×10^{-2} Hz
Cosmogenic ^{12}B and ^{12}N	1×10^{-2} Hz
Cosmogenic ^{7}B	6×10^{-3} Hz
Other cosmogenic long lived isotopes	6×10^{-3} Hz

is not available for online triggering purposes.

5.4 Background estimation

In table 5.1 we summarize the neutrino backgrounds for a supernova burst signal, while on table 5.2 we summarize the generic radioactive and cosmogenic background rates according to the evaluations made in the JUNO Yellow Book [34].

5.5 Simulation of the detector response

We examine the signal on each neutrino detection channel, evaluate its detection efficiency and compare it to the expected backgrounds. The time scale of the plots should be compared with the time spectrum in figure 2.2. As we have explained in the previous chapters, the electron neutrinos that are the main actors in the early phases of the supernova evolution are mostly converted to ν_x and as a consequence the charged current channels will be almost silent in the first $\sim 50 - 70$ ms.

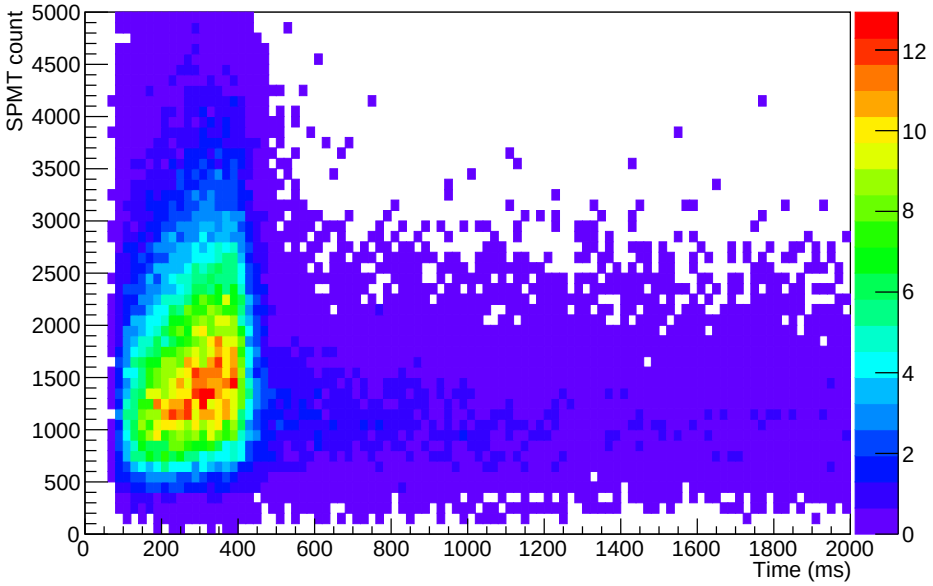

Figure 5.2: Inverse beta decay event rate in units of (200 PMT x 20 ms)$^{-1}$ for a 10 kpc SN neutrino burst.

5.5.1 Inverse beta decay

Figure 5.2 shows the event distribution versus time and SPMT count for a typical 10 kpc supernova neutrino burst at the JUNO detector. We can see that the IBD channel is silent in the first $\sim 50 - 70$ ms as expected, then the peak from the capture phase and the neutronization burst is clearly visible. We can also notice the increase in the emission temperature and the following decrease due to the core cooldown.

IBD events can be tagged by the time delayed coincidence between the prompt positron emission and the delayed neutron capture signal, with an average capture time of 250 μs as can be seen in figure 5.3.

Due to the double tagging the expected background rate of the IBD channel is small, as the rate reported in table 5.1 accounts for an average of 10^{-2} events in a ten second interval from reactor antineutrinos.

5.5.2 Proton elastic scattering

The proton elastic scattering spectrum, as expected, has a sharp fall on the SPMT count (energy) axis as can be seen in figure 5.4. The channel shows some interesting activity in the first 50 ms but since the energy of neutrinos emitted in the earlier stage of the supernova *capture phase* is low the proton

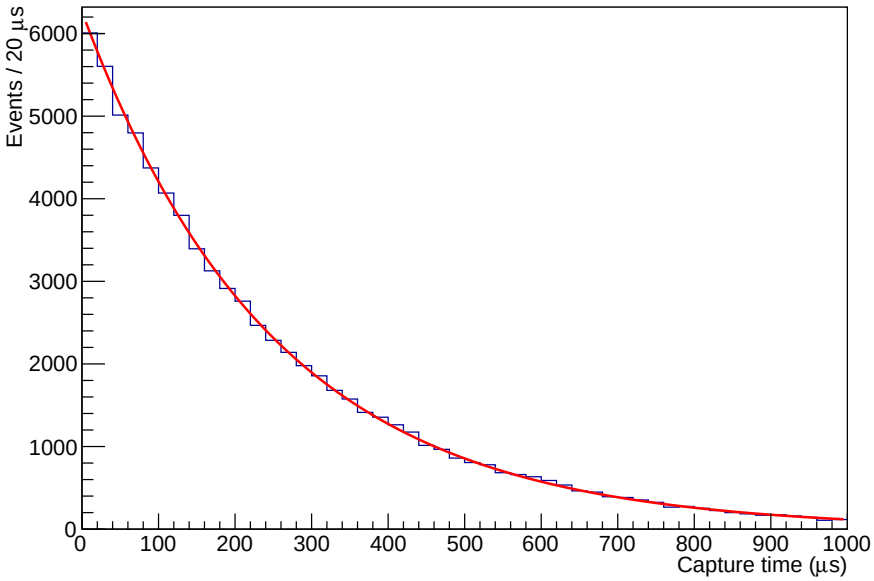

Figure 5.3: Neutron capture time for the IBD channel.

recoil energy falls under the rejection threshold.

The proton elastic scattering channels is more sensitive to backgrounds, being made of singles at low energy. The dominant background sources are the radioactive decays of scintillator materials and surroundings, accounting for a total rate estimated of $\sim 20\,\mathrm{Hz}$ by summing all the radioactivities over 0.2 MeV shown in table 5.2.

5.5.3 ^{12}C NC excitation

This channel is characterized by a monochromatic energy deposit of 15 MeV. From the plot in figure 5.5 we can notice that a small fraction of events gets detected with a lower energy if not actually lost due to the detector boundary effects. The channel is also silent in the early stage of the supernova, despite being neutral current, as the neutrinos emitted are well below the excitation process threshold shown in table 2.1.

The energy selection on 15.11 MeV photons for the ^{12}C NC channel identification can reject the main natural radioactivity background shown in table 5.2, that is negligible at this energy scale. IBD and superallowed CC events can be rejected as they are tagged by means of vertex and time correlation.

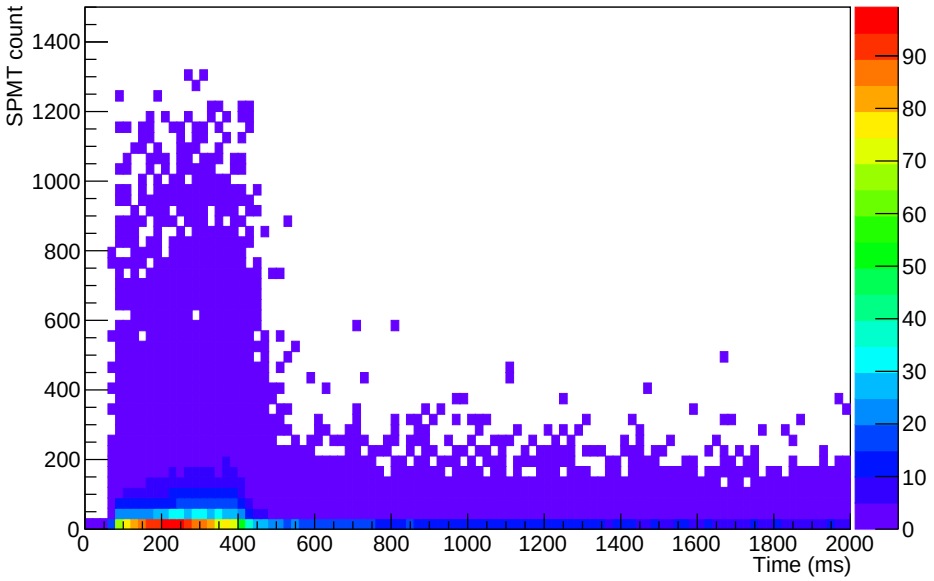

Figure 5.4: Proton elastic scattering event rate in units of (30 PMT x 20 ms)$^{-1}$ for a 10 kpc SN neutrino burst.

5.5.4 Electron elastic scattering

This channel is very interesting as it could provide a signature in the early stage of the supernova when the SN neutrino flux is dominated by ν_x (see the plot in fig. 2.2). The elastic scattering on electrons has an energy spectrum extending well over the dark noise level, as can be seen from the plot in fig. 5.6. Unfortunately due to the small cross section for this process, the interaction rate is higher than the natural radioactivity background (see table 5.2) only if the supernova is close enough to the Earth. We have simulated the early emission for a SN at 1 kpc yielding an average rate of 1 event per 10 ms against an average background of 0.1-0.2 events from natural radioactivity, but the signal falls to a level comparable to the background already for a SN at 2.5 kpc.

As for what is concerning the main emission phases, a higher energy threshold could suppress the natural radioactivities and further reduce the background to negligible levels. This strategy cannot be applied to the early phase, however, due to the small average energy of the neutrinos.

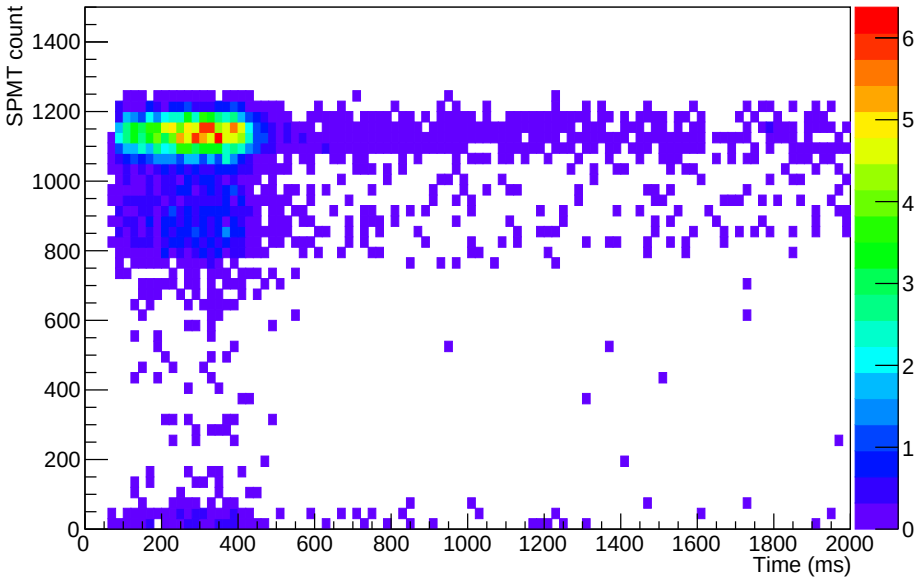

Figure 5.5: ^{12}C NC event rate in units of (30 PMT x 20 ms)$^{-1}$ for a 10 kpc SN neutrino burst.

5.5.5 Superallowed CC interactions

Event distribution for ^{12}B and ^{12}N superallowed CC primary interactions are shown in figures 5.7 and 5.8. Their signature is similar to the inverse beta decay channel, however the combination of a higher kinematic threshold and a lower cross section results in a much poorer statistics.

Identification of ^{12}B and ^{12}N events suffers from the much higher rate of the IBD prompt signal that may interfere in the tagging as the time window for the beta decay is of several hundreds of milliseconds, however a good rejection can be achieved through the correlation of prompt and delayed vertices correlation. Cosmogenic isotopes in a ten second interval are in the order of 10^{-1} both for ^{8}Li and ^{12}N / ^{12}B (see table 5.2) so they are assumed to be negligible.

5.6 Event rates and channel efficiencies

In table 5.3 we show the total event number and the estimated efficiency for each NC channel when applying a rejection of the events up to 30 hit SPMTs. For the charged current channels, the coincidence tagging has its own efficiency for which we based our estimate on the value reported in the JUNO Yellow Book [34] for the inverse beta decay process.

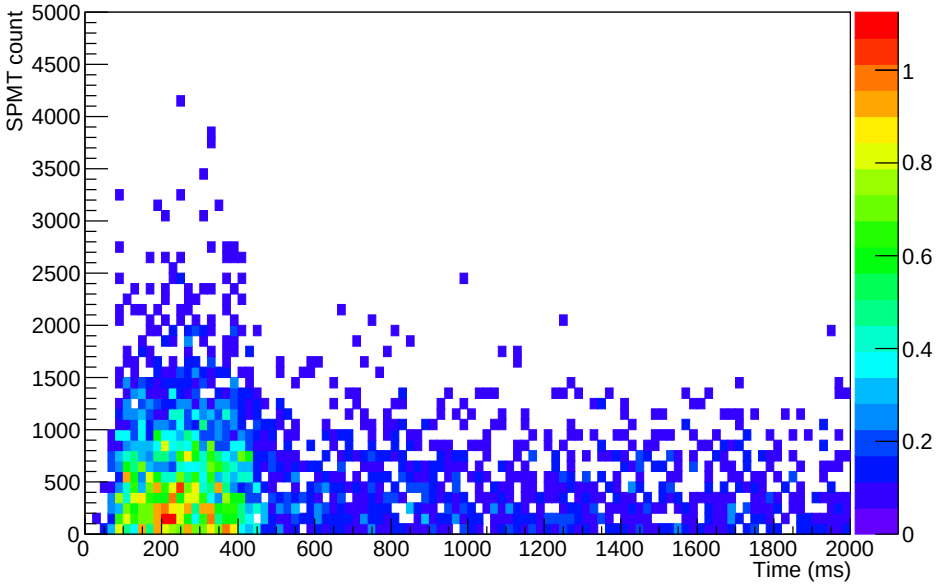

Figure 5.6: Electron elastic scattering event rate in units of (200 PMT x 20 ms)$^{-1}$ for a 10 kpc SN neutrino burst.

5.7 Energy calibration and resolution

Since the size of the detector is of the same order of magnitude of the scintillator attenuation length, the detector response depends on the event position, and this effect has to be taken in account when reconstructing the energy. Thanks to the spherical symmetry we can base the correction solely on the radius of the vertex position, with the resulting calibration profile is shown in figure 5.9.

We are using, as introduced in the previous chapters, the PMT count method where we evaluate the energy deposit by counting the number of the small PMTs being hit nad performing a Poisson correction according to equation 3.1.

The detected energy increases slowly as a function of the radius due to diminishing global attenuation losses, then undergoes a sharp drop around 16 meters due to onset of total reflection phenomena on the scintillator-acrylic interface.

We estimate the energy resolution of the SPMT system by evaluating the energy resolution at six different sample energies typically used for the energy calibration of the detector with radioactive sources and specific interaction signals with a monochromatic signature. The resolution as a function

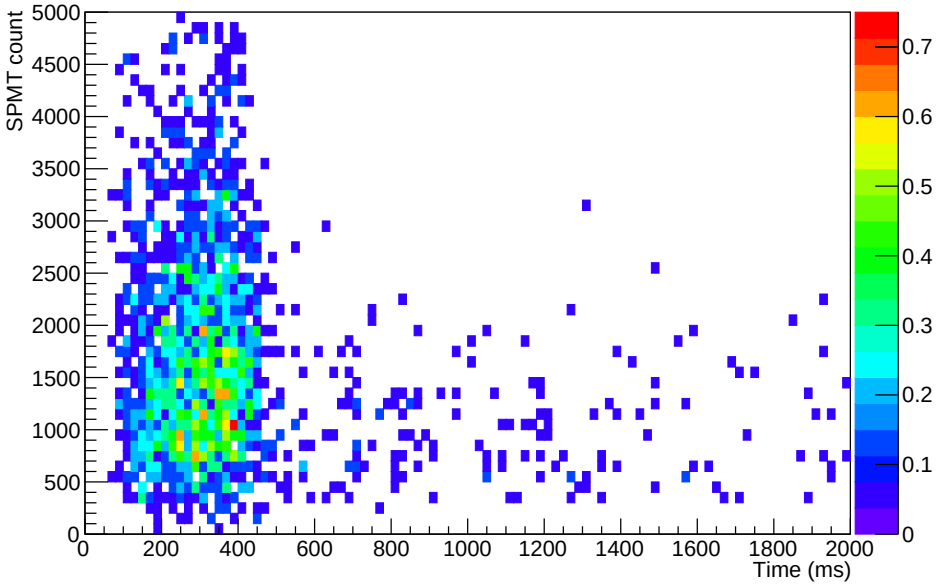

Figure 5.7: ^{12}B superallowed CC event rate in units of (200 PMT x 20 ms)$^{-1}$ for a 10 kpc SN neutrino burst.

of the energy is shown in figure 5.10 and be expressed as a function:

$$\frac{\sigma_E}{E} = \sqrt{\frac{a^2}{E} + b^2 + \frac{c^2}{E^2}}$$

where the fitting parameters are:

$$a = 1.04(5) \times 10^{-1};\ b = 2.5(4) \times 10^{-3};\ c = 4(1) \times 10^{-3}$$

5.8 Reconstructed spectra

In figure 5.11 we show in a single plot the energy spectrum of the SN neutrino channels reconstructed via the SPMT count method introduced in section 3.3, and integrated over time. In figure 5.12 we show a comparison between the reconstruction and the true energy. The noticeable discrepancy on the inverse beta decay interaction channel is still under investigation.

5.9 Data rate

An important point to evaluate in order to check for bottlenecks in the SPMT data flow is the data rate per single SPMT. As described in the

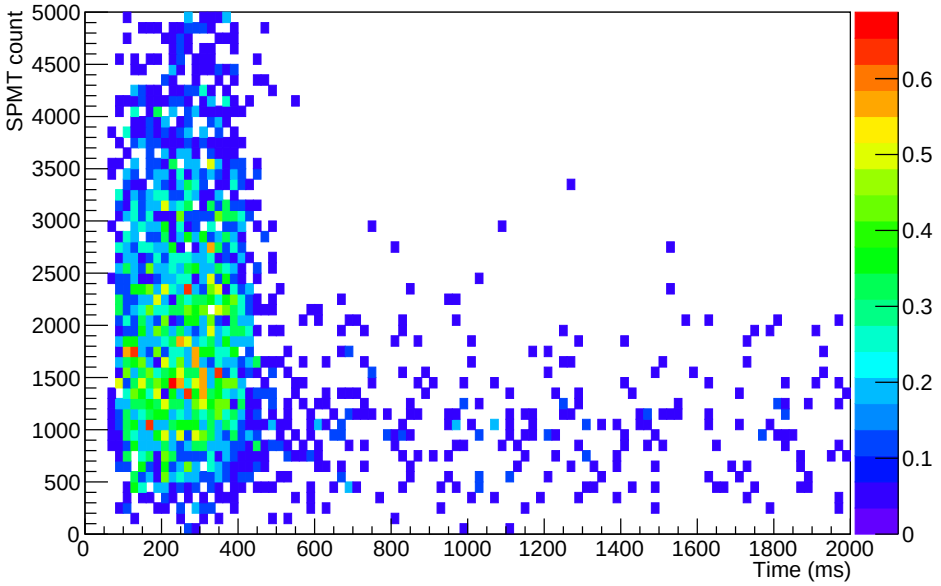

Figure 5.8: ^{12}N superallowed CC event rate in units of (200 PMT x 20 ms)$^{-1}$ for a 10 kpc SN neutrino burst.

third chapter, the SPMT readout is performed using the CatiROC chip, that produces a data output of 51 bit per hit channel.

From the plot in figure 5.13 we can estimate a peak of $\sim$ 40 kbit/s, accounting for a total of $\sim$ 1.5 Mbps when summed over the 36000 SPMTs. This rate is well within the foreseen bandwidth and it scales with the inverse square of the SN distance.

5.10 Asynchronous vs synchronous trigger

The CatiROC chip uses a ramp ADC for an analog to digital conversion that can be exploited alongside the digital readout. We will not take advantage of this capability in our analysis, but we still need to take in account the conversion time of 6.4 μs under which the electronic channel is blind. The dead time can introduce a bias in the reconstruction of the energy or the interaction rate, depending on the trigger strategy adopted for the readout. It also determines a maximum trigger rate given by the inverse of the dead time, i.e. $TR_{max} = (6.4\,\mu\text{s})^{-1} = 156$ kHz. On CatiROC chip, an analog memory system is implemented to buffer the signal during the acquisition window, theoretically providing the potential to increase the effective readout rate of a factor of two.

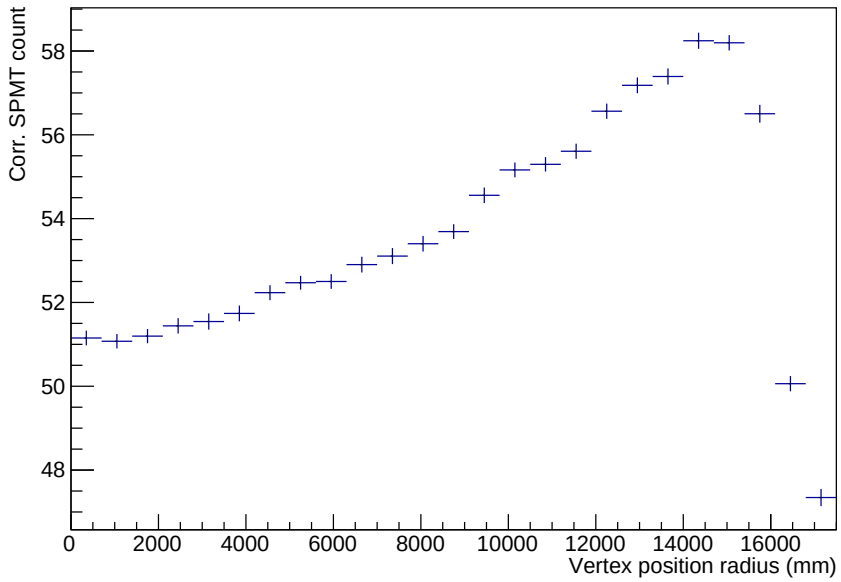

Figure 5.9: Number of hit SPMT (with Poisson correction) as a function of the radius per 1 MeV of energy deposit.

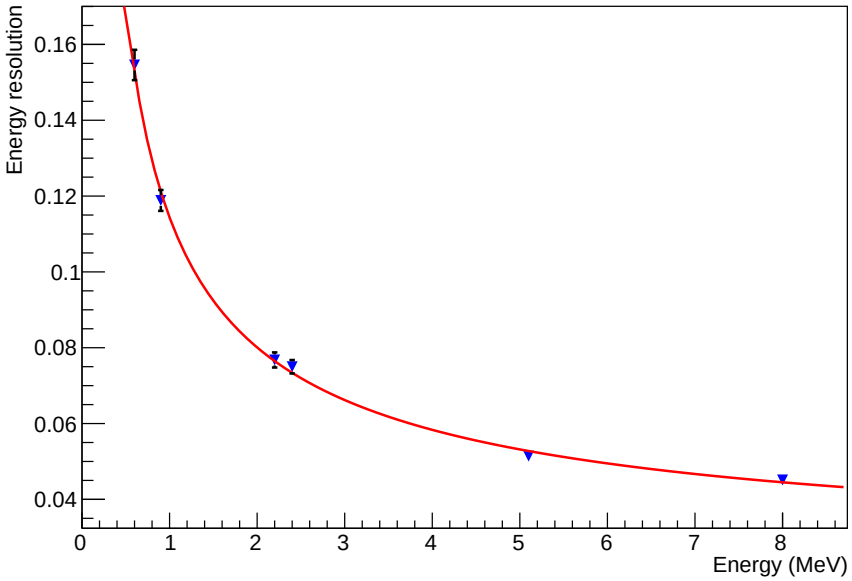

Figure 5.10: Energy resolution of the SPMT system.

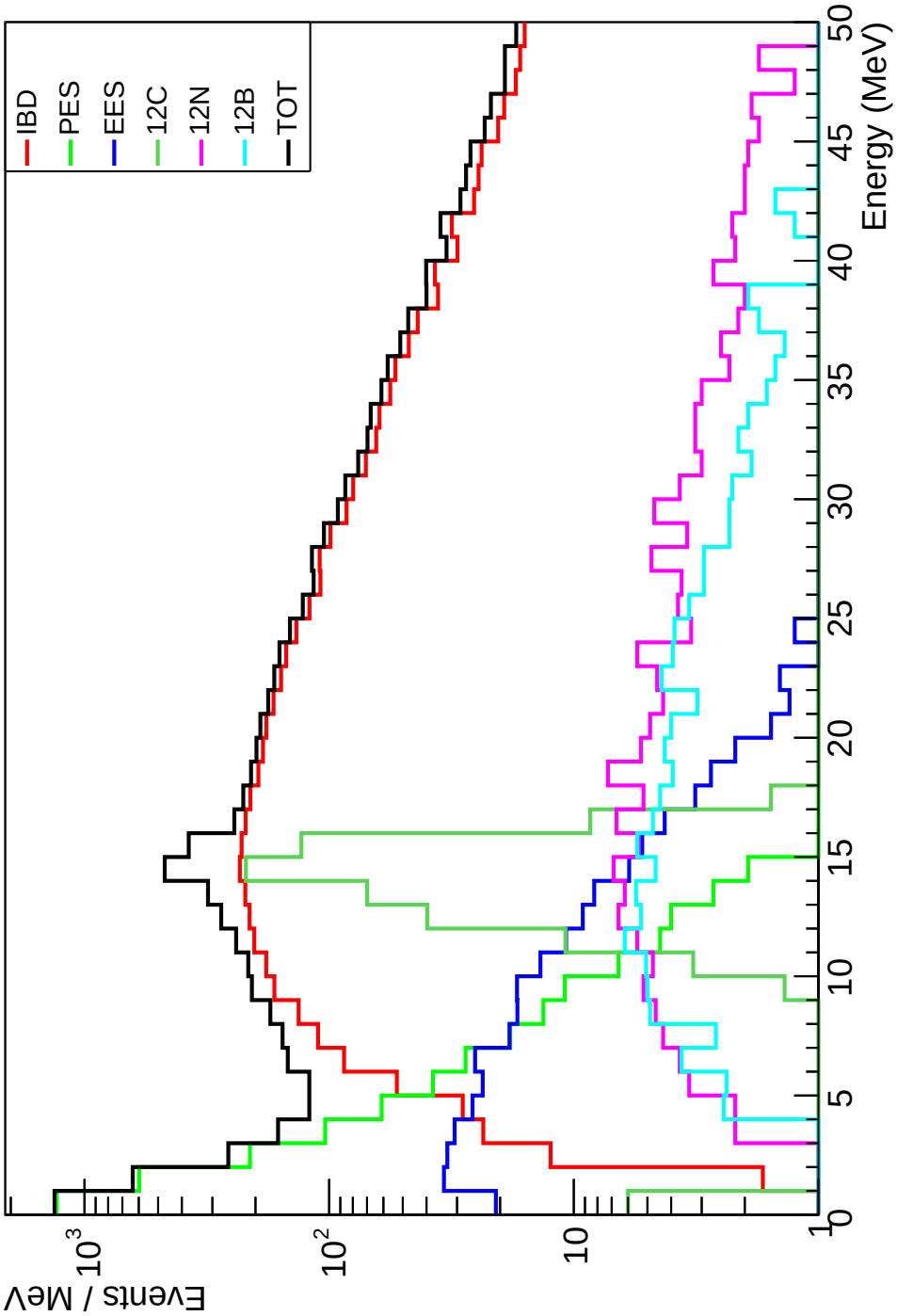

Figure 5.11: Reconstructed energy spetrum for all the SN neutrino channels for a 10 kpc SN.

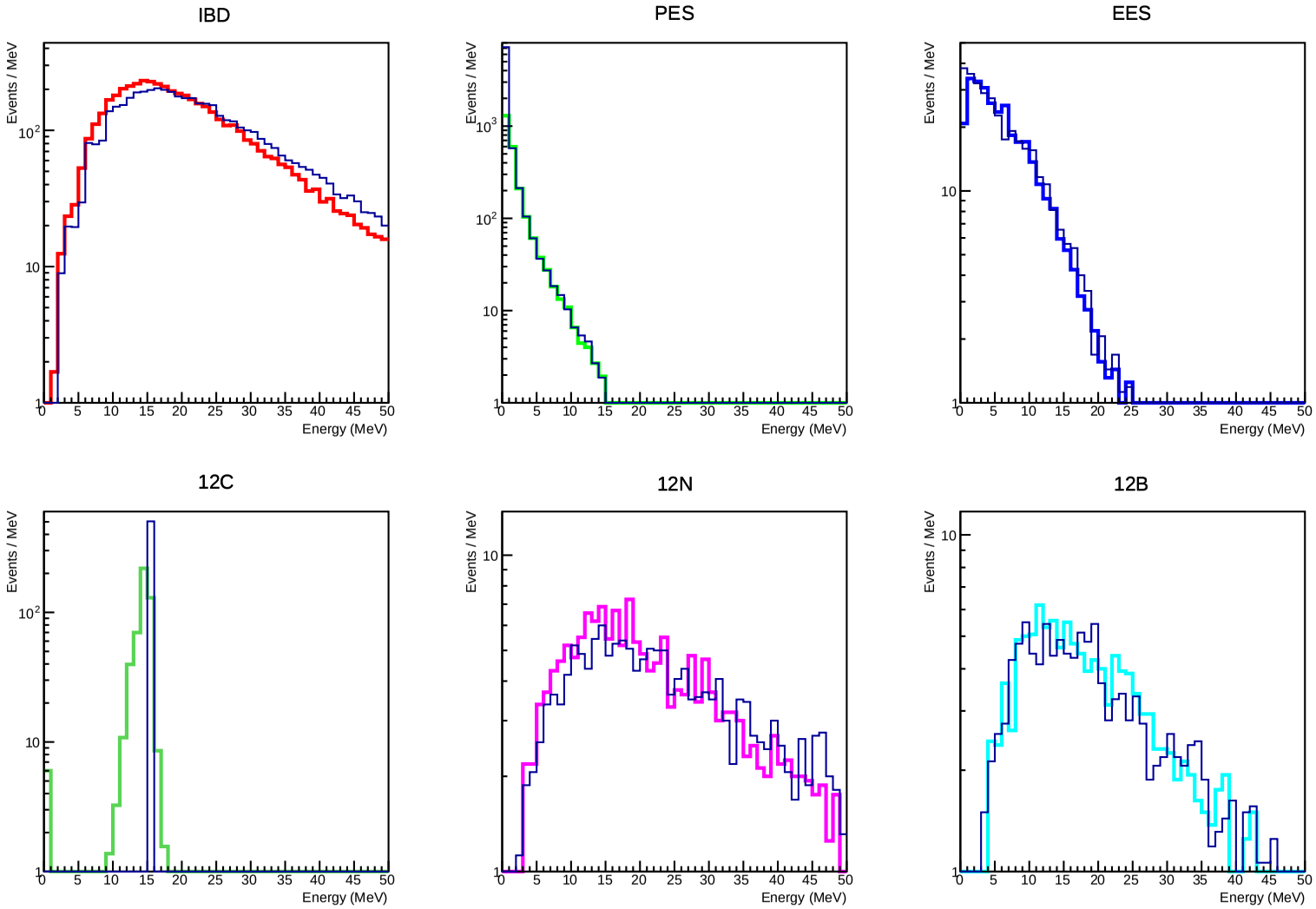

Figure 5.12: Comparison between true and reconstructed spectra for each SN neutrino channel for a 10 kpc SN.

Process	Events	Reconstructed events	Efficiency
Inverse beta decay (IBD)	$4.97(2) \times 10^3$	$3.62(2) \times 10^3$	73%
Proton elastic scattering	$7.96(2) \times 10^3$	$2.40(1) \times 10^3$	30%
Superallowed ^{12}C	$5.02(6) \times 10^2$	$4.95(6) \times 10^2$	99%
Electron elastic scattering	$3.37(5) \times 10^2$	$3.22(4) \times 10^2$	95%
Superallowed ^{12}N CC	$1.92(3) \times 10^2$	$1.40(3) \times 10^2$	73%
Superallowed ^{12}B CC	$1.38(3) \times 10^2$	$1.01(3) \times 10^2$	73%

Table 5.3: Summary of neutrino interaction channels in JUNO for a SN of 30 $M_\odot$ at 10 kpc.

In the case of an asynchronous trigger for the small PMTs, a bias in the reconstruction of the energy is introduced when two vertices are near enough in space and time to illuminate the same subset of photomultipliers within the dead time window. In the case of a synchronous system, the trigger is global and the second event is rejected if it falls within the system dead time. This causes a loss of detected events eventually producing an error in the reconstruction on the rate, while no bias in the reconstruction of the energy is expected.

We have simulated the error in the energy reconstruction of the inverse beta decay prompt emission introduced by the effect of the dead time of the single photomultipliers, in the case of a near SN at 2.5 kpc. The result is shown in figure 5.14 from which we can estimate an average error of $\sim 3\%$.

For the synchronous case, we have simulated the effect of the dead time on the reconstruction of the interaction rate and performed a correction of the observed rate by means of a polynomial function. As it can be seen in figure 5.15, such correction can provide good results. In figure 5.16 we summarize the rate reconstruction error as a function of the time within the burst and the supernova distance, from which we can evaluate that the reconstruction is accurate within a few percents.

5.11 Supernova trigger strategies

We are interested in defining a trigger strategy for the early identification of a supernova burst in order to change the detector readout strategy as needed to acquire the event set with the maximum available performance.

Figure 5.17 shows the total rate of events above the 30 SPMT count threshold in the first 100 ms. The background rate is dominated by natural radioactivities and can be assumed to be on the order of 20 Hz, giving an average of 2 events per 100 ms. By means of a Monte Carlo test we can estimate, assuming a supernova trigger threshold of 15 events within 100 ms, a fake trigger rate of 1.1 per year, which is deemed acceptable.

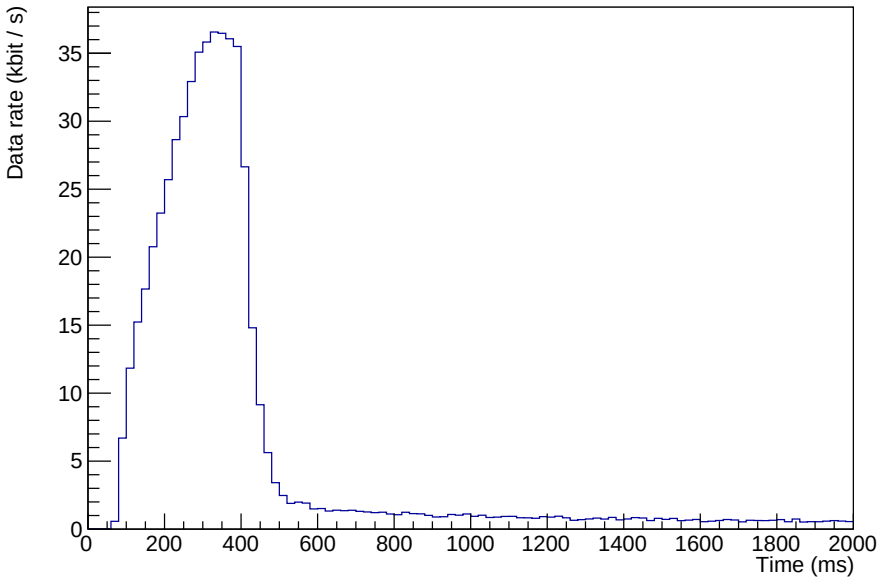

Figure 5.13: Average data rate on the single SPMT electronic channel for a SN at 10 kpc.

A different strategy can be implemented by generating a trigger when at least five event are detected over the 500 SPMT count threshold (approx. 10 MeV), in order to suppress the background from natural radioactivities, reactor neutrinos and geoneutrinos. The event rate in the first 100 ms is shown in figure 5.18 and we can see that with such strategy the SN can be triggered between 70 and 80 ms (i.e. 30 ms after the onset of the collapse).

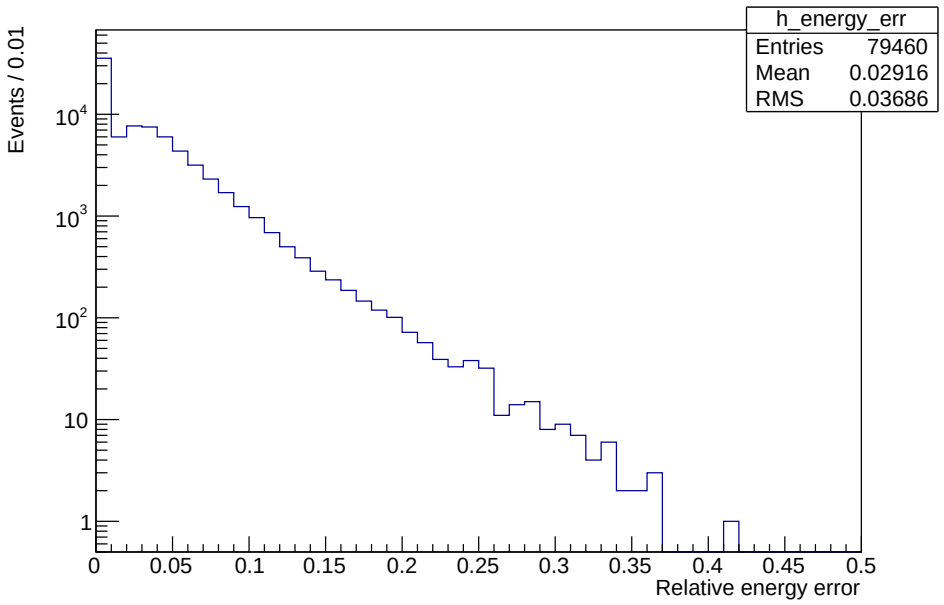

Figure 5.14: Event rate as a function of the error in the energy reconstruction introduced by the SPMT dead time for a SN at 2.5 kpc.

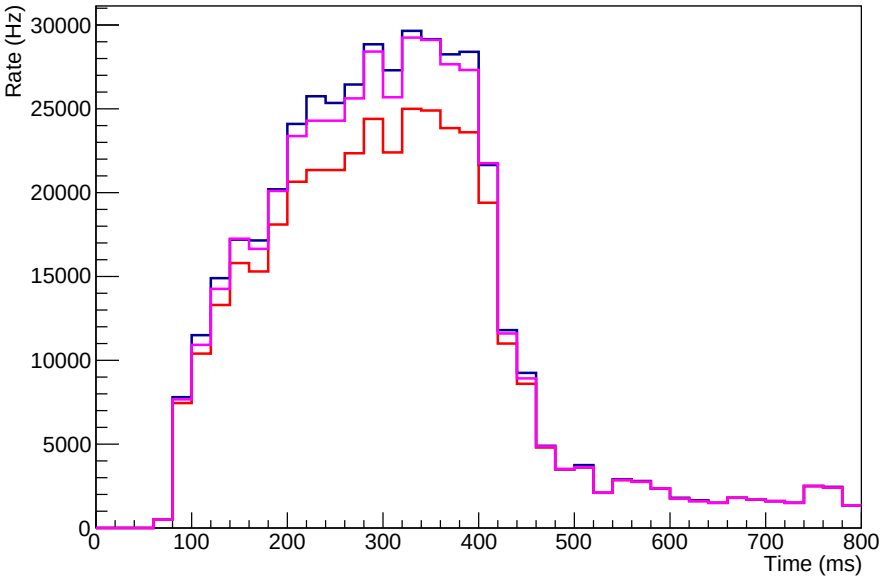

Figure 5.15: Comparison of the true rate (blue), observed rate (fuxia) and corrected observed rate (red) for the peak interaction rate of a SN at 10 kpc.

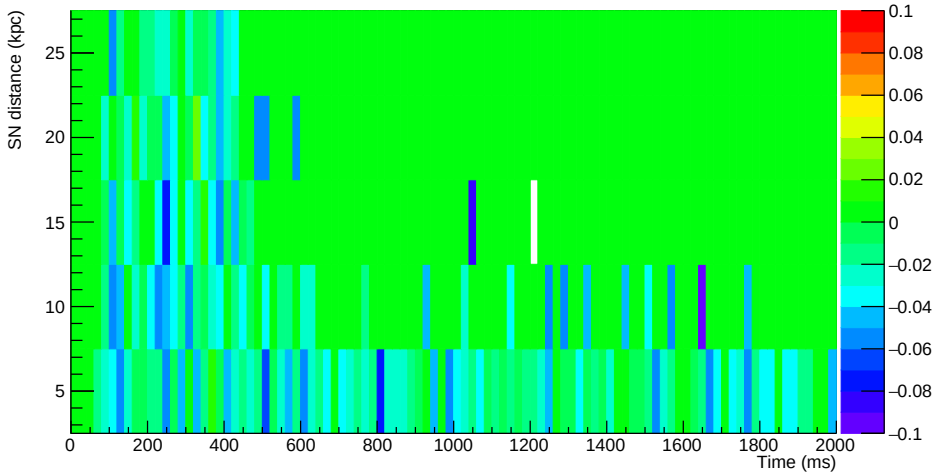

Figure 5.16: Error in the rate reconstruction as a function of time within the burst and the distance of the supernova.

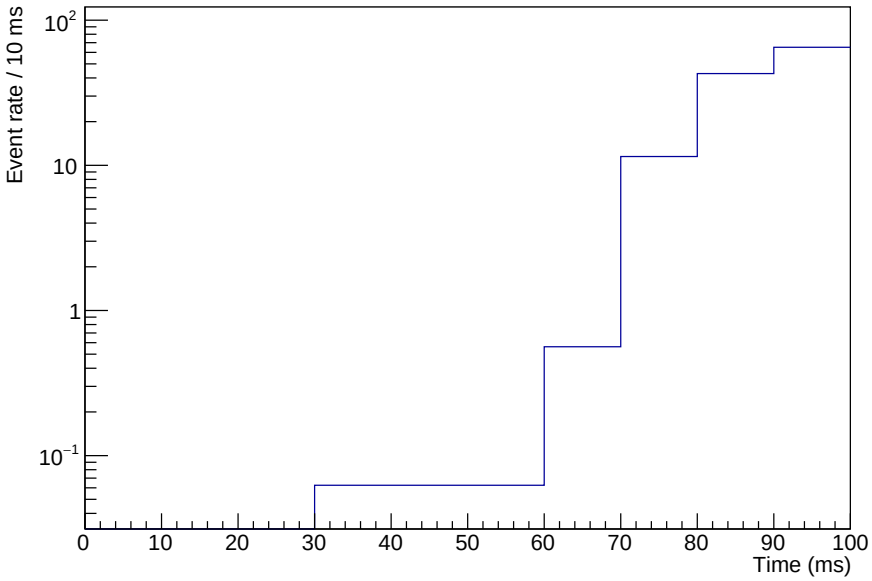

Figure 5.17: Rate of events over the 30 SPMT threshold in the first 100 ms for a SN at 10 kpc.

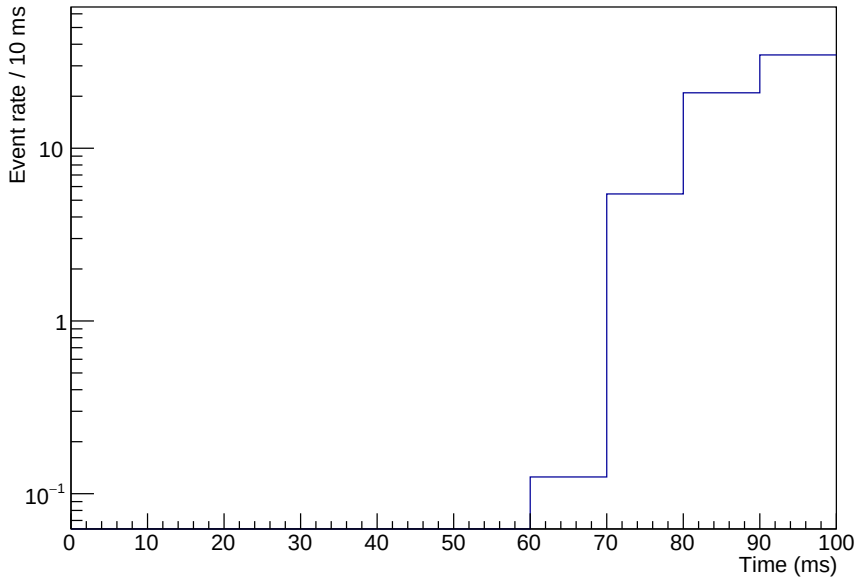

Figure 5.18: Rate of events over the 500 SPMT threshold in the first 100 ms for a SN at 10 kpc.

Chapter 6

Conclusions

Within this thesis, we have evaluated the potential for the study of a supernova neutrino burst with the small PMT system of the JUNO detector.

We have combined two existing software tools - a Supernova Monte Carlo generator and a GEANT4 simulation of the JUNO detector - to simulate the response of the system to a supernova neutrino burst.

We have characterized the detector response for the small PMT system in order to define a coincidence threshold within a proper time window for the identification of the events over the dark noise background.

We have shown the detector response on the six most relevant channels for the detection of SN neutrinos in liquid scintillator: three charged current (inverse beta decay and superallowed ^{12}C and ^{12}B) sensitive to the electronic neutrinos and three neutral current (proton and electron elastic scattering and ^{12}C excitation) sensitive to the overall emission on all flavors. For each channel we examined the background rate which is usually negligible when compared to the peak signal magnitude but becomes significant when the early stage of the supernova evolution is examined.

We have estimated the reconstruction efficiency for each channel: the number of reconstructed events is reduced mainly due to the tagging inefficiency of the inverse beta decay signal and the loss of the low energy peak on the proton elastic scattering spectrum.

The simulated data has been used to evaluate potential bottlenecks in the readout system: we have estimated the global and average-per-channel data rates for the small PMT system.

We have compared the effects of the photomultiplier readout dead time on the energy reconstruction in the case of an asynchronous trigger strategy and on the rate reconstruction in the case of a synchronous trigger for the SPMT system readout.

We have proposed two possible trigger mechanisms for the early detection of the SN burst, both successful in triggering the supernova signal shortly after the onset of the collapse.

Bibliography

[1] W. Baade and F. Zwicky. Remarks on super-novae and cosmic rays. *Phys. Rev.*, 46:76–77, 1934.

[2] Saul A. Teukolsky and Stuart L. Shapiro. *Black holes, white dwarfs, and neutron stars : the physics of compact objects*. Wiley, 1983.

[3] S. E. Woosley and T. A. Weaver. The physics of supernova explosions. *Ann. Rev. Astron. Astrophys.*, 24:205, 1986.

[4] M. M. Phillips. The absolute magnitudes of Type IA supernovae. *The Astrophysical Journal, Letters*, 413:L105–L108, August 1993.

[5] E. Cappellaro and M. Turatto. Supernova types and rates. *Astrophys.Space Sci.Libr.*, 264:199, 2001. The Influence of Binaries on Stellar Population Studies, Brussels 21-25 Aug. 2000.

[6] C. Giunti and C. W. Kim. *Fundamentals of Neutrino Physics and Astrophysics*. Oxford University Press, Oxford, UK, 2007.

[7] F. Mannucci et al. The supernova rate in local galaxy clusters. *Mon. Not. Roy. Astron. Soc.*, 383:1121–1130, 2008.

[8] B. Cameron Reed. New estimates of the solar-neighborhood massive-stars birthrate and the galactic supernova rate. *Astronomical J.*, 130:1652–1657, 2005.

[9] E.N. Alexeyev and L.N. Alexeyeva. Twenty years of galactic observations in searching for bursts of collapse neutrinos with the Baksan Underground Scintillation Telescope. *J. Exp. Theor. Phys.*, 95:5, 2002.

[10] M. Malek et al. Search for supernova relic neutrinos at Super-Kamiokande. *Phys. Rev. Lett.*, 90:061101, 2003.

[11] H. Thomas Janka et al. Core-collapse supernovae: Reflections and directions. *PTEP*, 2012:01A309, 2012.

[12] A. Heger, C. L. Fryer, S. E. Woosley, N. Langer, and D. D H Hartmann. How massive single stars end their life. *Astrophysical Journal*, 591(1 I):288–300, 1 2003.

[13] Adam Burrows, Klein Klein, and Raj Gandhi. The future of supernova neutrino detection. *Phys. Rev. D*, 45:3361–3385, May 1992.

[14] Todd A. Thompson, Adam Burrows, and Philip A. Pinto. Shock breakout in core-collapse supernovae and its neutrino signature. *Astrophys. J.*, 592:434, 2003.

[15] T. Totani, K. Sato, H. E. Dalhed, and J. R. Wilson. Future detection of supernova neutrino burst and explosion mechanism. *Astrophys. J.*, 496:216–225, 1998.

[16] George Sonneborn, Bruce Altner, and Robert P. Kirshner. The progenitor of SN 1987A - Spatially resolved ultraviolet spectroscopy of the supernova field. *Astrophys. J.*, 323:L35–L39, 1987.

[17] J. Middleditch et al. A 2.14 ms candidate optical pulsar in SN1987A. 2000. 5th CTIO/ESO Workshop and 1st CTIO/ESO/LCO Workshop: SN 1987A: Ten Years After, La Serena, Chile, 22-28 Feb 1997.

[18] M. Aglietta et al. Neutrino astrophysics and SN1987A. *Nuovo Cim.*, C13:365–374, 1990.

[19] A. De Rujula. May a supernova bang twice? *Phys. Lett.*, B193:514, 1987.

[20] K. S. Hirata et al. Observation in the Kamiokande-II detector of the neutrino burst from supernova sn1987a. *Phys. Rev.*, D38:448–458, 1988.

[21] Thomas J. Loredo and Don Q. Lamb. Bayesian analysis of neutrinos observed from supernova sn 1987a. *Phys. Rev.*, D65:063002, 2002.

[22] Cristina Volpe. Open issues in neutrino astrophysics. *Annalen der Physik*, 525(8-9):588–599, 2013.

[23] Amol S. Dighe and Alexei Yu. Smirnov. Identifying the neutrino mass spectrum from the neutrino burst from a supernova. *Phys. Rev.*, D62:033007, 2000.

[24] S. H. Chiu, Chu-Ching Huang, and Kwang-Chang Lai. Signatures of the neutrino mass hierarchy in supernova neutrinos. *PTEP*, 2015:063, 2013.

[25] David N. Schramm. Neutrinos from supernova SN1987A. *Comments Nucl. Part. Phys.*, 17:239, 1987.

[26] A. B. Balantekin, J. Gava, and C. Volpe. Possible CP-violation effects in core-collapse supernovae. *Phys. Lett.*, B662:396–404, 2008.

[27] K. Scholberg. The supernova early warning system. *Astronomische Nachrichten*, 329(3):337–339, 2008.

[28] Irene Tamborra, Bernhard Müller, Lorenz Hüdepohl, Hans-Thomas Janka, and Georg Raffelt. High-resolution supernova neutrino spectra represented by a simple fit. *Phys. Rev. D*, 86:125031, Dec 2012.

[29] G. Pagliaroli, F. Vissani, M. L. Costantini, and A. Ianni. Improved analysis of SN1987A antineutrino events. 2008.

[30] C. Lujan-Peschard, G. Pagliaroli, and F. Vissani. Spectrum of supernova neutrinos in ultra-pure scintillators. *JCAP*, 1407:051, 2014.

[31] Ken'ichiro Nakazato, Kohsuke Sumiyoshi, Hideyuki Suzuki, Tomonori Totani, Hideyuki Umeda, and Shoichi Yamada. Supernova neutrino light curves and spectra for various progenitor stars: From core collapse to proto-neutron star cooling. *The Astrophysical Journal Supplement Series*, 205(1):2, 2013.

[32] G. Bellini et al. Observation of geo-neutrinos. *Phys. Lett.*, B687:299–304, 2010.

[33] T. Adam et al. JUNO Conceptual Design Report. 2015.

[34] Fengpeng An et al. Neutrino physics with juno. *J. Phys.*, G43:030401, 2016.

[35] T. Adam et al. The OPERA experiment target tracker. *Nucl.Instrum.Meth.*, A577:523–539, 2007.

[36] L. Classen and O. Kalekin. Status of the PMT development for KM3NeT. *Nucl. Instrum. Meth.*, A725:155–157, 2013.

[37] S. Agostinelli et al. GEANT4: A Simulation toolkit. *Nucl. Instrum. Meth.*, A506:250–303, 2003.

[38] M. Dobbs and J.B. Hansen. The HepMC C++ Monte Carlo event record for high energy physics. *Comput. Phys. Commun.*, 134:41–46, 2001.

[39] Kate Scholberg. Supernova neutrino detection. *J. Phys. Conf. Ser.*, 375:042036, 2012.

[40] Cristina Volpe. Neutrino astrophysics : recent advances and open issues. *J. Phys. Conf. Ser.*, 631:012048, 2015. DISCRETE 2014.

[41] Steen Hannestad, Georg G. Raffelt, Günter Sigl, and Yvonne Y. Y. Wong. Self-induced conversion in dense neutrino gases: Pendulum in flavor space. *Phys. Rev. D*, 74:105010, Nov 2006.